

# VALES VI: ISM enrichment in star-forming galaxies up to $z \sim 0.2$ using $^{12}\text{CO}(1-0)$ , $^{13}\text{CO}(1-0)$ , and $\text{C}^{18}\text{O}(1-0)$ line luminosity ratios

H. Méndez-Hernández<sup>1</sup>,<sup>★</sup> E. Ibar<sup>1</sup> K. K. Knudsen<sup>2</sup>,<sup>3</sup> P. Cassata<sup>3,4</sup> M. Aravena<sup>5</sup>  
M. J. Michałowski<sup>6</sup>,<sup>7</sup> Zhi-Yu Zhang<sup>8</sup>,<sup>9</sup> M. A. Lara-López<sup>9</sup>, R. J. Ivison<sup>10</sup> P. van der Werf<sup>11</sup>  
V. Villanueva<sup>12</sup> R. Herrera-Camus<sup>13</sup> and T. M. Hughes<sup>1,14,15,16</sup>

<sup>1</sup>Instituto de Física y Astronomía, Universidad de Valparaíso, Avda. Gran Bretaña 1111, 2340000 Valparaíso, Chile

<sup>2</sup>Department of Space, Earth and Environment, Chalmers University of Technology, Onsala Space Observatory, SE-439 92 Onsala, Sweden

<sup>3</sup>Dipartimento di Fisica e Astronomia Galileo Galilei, Università degli Studi di Padova, Vicolo dell'Osservatorio 3, I-35122 Padova Italy

<sup>4</sup>INAF Osservatorio Astronomico di Padova, Vicolo dell'Osservatorio 5, I-35122 Padova, Italy

<sup>5</sup>Núcleo de Astronomía, Facultad de Ingeniería y Ciencias, Universidad Diego Portales, Av. Ejército Libertador 441, Santiago 8370191, Chile

<sup>6</sup>Astronomical Observatory Institute, Faculty of Physics, Adam Mickiewicz University, ul. Słoneczna 36, PL-60-286 Poznań, Poland

<sup>7</sup>Key Laboratory of Modern Astronomy and Astrophysics, Nanjing University, Ministry of Education, Nanjing 210093, China

<sup>8</sup>School of Astronomy and Space Science, Nanjing University, Nanjing 210093, China

<sup>9</sup>DARK, Niels Bohr Institute, University of Copenhagen, Lyngbyvej 2, Copenhagen DK-2100, Denmark

<sup>10</sup>European Southern Observatory, Alonso de Córdova, 3107, Vitacura, Santiago 763-0355, Chile

<sup>11</sup>Leiden Observatory, Leiden University, PO Box 9513, NL-2300 RA Leiden, the Netherlands

<sup>12</sup>Department of Astronomy, University of Maryland, College Park, MD 20742, USA

<sup>13</sup>Department of Astronomy, Faculty of Physical and Mathematical Sciences, Universidad de Concepción, Esteban Iturría Avenue (unnumbered) Barrio Universitario 160-C, Concepción, Chile

<sup>14</sup>Chinese Academy of Sciences South America Center for Astronomy, China-Chile Joint Center for Astronomy, Camino El Observatorio #1515, Las Condes, Santiago Casilla 36-D, Chile

<sup>15</sup>CAS Key Laboratory for Research in Galaxies and Cosmology, Department of Astronomy, University of Science and Technology of China, Hefei 230026, China

<sup>16</sup>School of Astronomy and Space Science, University of Science and Technology of China, Hefei 230026, China

Accepted 2020 June 29. Received 2020 June 1; in original form 2019 December 4

## ABSTRACT

We present Atacama Large Millimeter/sub-millimeter Array (ALMA) observations towards 27 low-redshift ( $0.02 < z < 0.2$ ) star-forming galaxies taken from the Valparaíso ALMA/APEX Line Emission Survey. We perform stacking analyses of the  $^{12}\text{CO}(1-0)$ ,  $^{13}\text{CO}(1-0)$ , and  $\text{C}^{18}\text{O}(1-0)$  emission lines to explore the  $L' [^{12}\text{CO}(1-0)]/L' [^{13}\text{CO}(1-0)]$  [hereafter  $L' (^{12}\text{CO})/L' (^{13}\text{CO})$ ] and  $L' [^{13}\text{CO}(1-0)]/L' [\text{C}^{18}\text{O}(1-0)]$  [hereafter  $L' (^{13}\text{CO})/L' (\text{C}^{18}\text{O})$ ] line luminosity ratio dependence as a function of different global galaxy parameters related to the star formation activity. The sample has far-IR luminosities of  $10^{10.1-11.9} L_{\odot}$  and stellar masses of  $10^{9.8-10.9} M_{\odot}$  corresponding to typical star-forming and starburst galaxies at these redshifts. On average, we find an  $L' (^{12}\text{CO})/L' (^{13}\text{CO})$  line luminosity ratio value of  $16.1 \pm 2.5$ . Galaxies with pieces of evidence of possible merging activity tend to show higher  $L' (^{12}\text{CO})/L' (^{13}\text{CO})$  ratios by a factor of 2, while variations of this order are also found in galaxy samples with higher star formation rates (SFRs) or star formation efficiencies (SFEs). We also find an average  $L' (^{13}\text{CO})/L' (\text{C}^{18}\text{O})$  line luminosity ratio of  $2.5 \pm 0.6$ , which is in good agreement with those previously reported for starburst galaxies. We find that galaxy samples with high  $L_{\text{IR}}$ , SFR, and SFE show low  $L' (^{13}\text{CO})/L' (\text{C}^{18}\text{O})$  line luminosity ratios with high  $L' (^{12}\text{CO})/L' (^{13}\text{CO})$  line luminosity ratios, suggesting that these trends are produced by selective enrichment of massive stars in young starbursts.

**Key words:** methods: statistical – techniques: interferometric – galaxies: star formation – galaxies: ISM.

## 1 INTRODUCTION

Stars are mostly formed within Giant Molecular Clouds (GMCs), cold dense regions of the interstellar medium (ISM), which are characterized by high densities ( $n_{\text{H}_2} > 10^4 \text{ cm}^{-3}$ ; Gao & Solomon 2004; Bergin & Tafalla 2007) and low temperatures (10–20 K; Evans 1999) that favour the formation of stars. In these regions, the most abundant molecule is molecular hydrogen,  $\text{H}_2$ ; however, its lack of a permanent

electric dipole makes it difficult to observe in emission. After  $\text{H}_2$ , the next most abundant molecule is carbon monoxide,  $^{12}\text{C}^{16}\text{O}$  (hereafter CO), which easily emits photons from low-level rotational transitions in similar ISM conditions as those in which the  $\text{H}_2$  molecule resides. Therefore, the CO emission from low- $J$  rotational transitions has become the workhorse tracer of the  $\text{H}_2$  gas mass in the Local Universe and beyond (Bolatto, Wolfire & Leroy 2013).

Since the CO emission is mostly optically thick within GMCs, optically thin CO isotopologues are usually used to look deeper into the densest regions of GMCs. Since  $^{12}\text{C}$ ,  $^{16}\text{O}$ , and their isotopes,  $^{13}\text{C}$  and  $^{18}\text{O}$ , are mainly products of primary and secondary stellar nucle-

\* E-mail: hugo.mendez@postgrado.uv.cl

osynthesis processes, they are powerful tracers of the evolutionary state of a galaxy, and represent excellent tools to characterize the physical conditions and the chemical processes of the ISM (Wilson & Rood 1994; Milam et al. 2005; Romano et al. 2017). Narayanan & Krumholz (2014) showed that alongside gas density and temperature, the optical depth from low- $J$  CO lines is well correlated with the star formation rate (SFR) surface density of GMCs. Moreover, it is possible to trace different stellar nucleosynthesis scenarios, by comparing  $^{12}\text{CO}$ ,  $^{13}\text{CO}$ , and  $\text{C}^{18}\text{O}$  abundance variations. For example, Henkel & Mauersberger (1993) showed that dense regions that recently experienced a star formation event are expected to have higher abundances of  $\text{C}^{18}\text{O}$  and  $^{12}\text{CO}$  compared to  $^{13}\text{CO}$ . The  $^{12}\text{C}/^{13}\text{C}$  abundance ratio reflects the relative degree of primary to secondary nucleosynthesis processing, while the  $^{18}\text{O}/^{16}\text{O}$  abundance ratio traces differences in the initial mass function (IMF; Milam et al. 2005; Romano et al. 2017). In practice, albeit the optical depth effects, we could assume that the  $^{12}\text{C}/^{13}\text{C}$  and  $^{18}\text{O}/^{16}\text{O}$  abundance ratios can be traced by the molecular  $I(^{12}\text{CO})/I(^{13}\text{CO})$  and  $I(^{13}\text{CO})/I(\text{C}^{18}\text{O})$  line intensity ratios, respectively.

After the first detection of  $^{12}\text{CO}$  and its isotopologues in the Milky Way (Wilson, Jefferts & Penzias 1970; Penzias, Jefferts & Wilson 1971), several works have repeated their detection in nearby galaxies (Rickard et al. 1975; Encarnaz et al. 1979; Rickard & Blitz 1985; Young & Sanders 1986). More recently, several works have proven successfully the usage of  $I(^{12}\text{CO})/I(^{13}\text{CO})$  and  $I(^{13}\text{CO})/I(\text{C}^{18}\text{O})$  line ratios in nearby galaxies (Jiménez-Donaire et al. 2017; Sliwa et al. 2017; Cormier et al. 2018; Brown & Wilson 2019) and lensed high-redshift galaxies (Henkel et al. 2010; Danielson et al. 2013; Spilker et al. 2014; Zhang et al. 2018).

An environmental dependence for  $^{12}\text{C}/^{13}\text{C}$  has been shown by Alatalo et al. (2015), who found that 17 early-type galaxies (ETGs) located in the Virgo cluster and groups showed a line intensity ratio about two times lower than that of field galaxies. They proposed three different scenarios in which the observed variations could be explained: an extra low-mass stellar enrichment taking place in Virgo cluster galaxies, an increased mid-plane pressure effects of the intracluster medium (ICM), or the survival of only the densest clumps of molecular clouds as galaxies enter the ICM. Additionally, Davis (2014) showed a systematic dependence of the  $I(^{12}\text{CO})/I(^{13}\text{CO})$  line intensity ratio on the SFR surface density ( $\Sigma_{\text{SFR}}$ ) and the molecular gas surface density ( $\Sigma_{\text{H}_2}$ ) using a sample of nearby starburst and ETGs. They suggest that the observed correlations are caused by the combined action of massive stars heating and/or inducing turbulence in the gas phase of those galaxies with higher  $\Sigma_{\text{SFR}}$ .

Recent works have reported  $I(^{13}\text{CO})/I(\text{C}^{18}\text{O})$  line intensity ratios for different galaxy types. Danielson et al. (2013) showed a low  $I(^{13}\text{CO})/I(\text{C}^{18}\text{O})$  line intensity ratio ( $\sim 1$ ) in a high-redshift lensed galaxy suggesting the presence of a significant fraction of high-mass stars. Sliwa et al. (2017) reported a simultaneous high  $I(^{12}\text{CO})/I(^{13}\text{CO})$  ( $\gg 60$ ) intensity ratio with a low  $I(^{13}\text{CO})/I(\text{C}^{18}\text{O})$  ( $\lesssim 1$ ) intensity ratio consistent with an ISM enrichment by the presence of a young starburst, a top-heavy IMF, or their combined action. Jiménez-Donaire et al. (2017) presented an  $I(^{13}\text{CO})/I(\text{C}^{18}\text{O})$  line intensity ratio dependence with  $\Sigma_{\text{SFR}}$  and galactocentric distance in nine nearby spiral galaxies due to the selective enrichment of the ISM by massive stars. More recently, Zhang et al. (2018) showed high  $I(^{12}\text{CO})/I(^{13}\text{CO})$  line intensity ratios with a simultaneous low  $I(^{13}\text{CO})/I(\text{C}^{18}\text{O})$  line intensity ratio in four gravitationally lensed sub-millimetre galaxies (SMGs) at  $z \sim 2-3$ , and claimed this to be caused by a change of the IMF where there is a higher number of massive stars in high- $z$  starburst galaxies than in typical galaxies.

For galaxies beyond the Local Universe, the observation of faint emission lines as  $^{13}\text{CO}$  or  $\text{C}^{18}\text{O}$  is usually challenging. The abundances of  $^{13}\text{CO}$  and  $\text{C}^{18}\text{O}$  are typically 50 and 500 times lower than those of  $^{12}\text{CO}$  (Jiménez-Donaire et al. 2017) and their flux density ratios usually range between 20 and 100 for  $I(^{12}\text{CO})/I(^{13}\text{CO})$  and between 20 and 140 for  $I(^{12}\text{CO})/I(\text{C}^{18}\text{O})$  (Aalto et al. 1991; Casoli, Dupraz & Combes 1992b; König et al. 2016; Sliwa et al. 2017). For individual detections in nearby local ultra-luminous infrared galaxies (ULIRGs),  $^{13}\text{CO}$  and  $\text{C}^{18}\text{O}$  observations need to be at least four times deeper than  $^{12}\text{CO}$  observations to yield line detections (Sliwa et al. 2017; Brown & Wilson 2019). In this work, we propose an alternative way to overcome sensitivity limitations by stacking the signals of the  $^{12}\text{CO}(1-0)$ ,  $^{13}\text{CO}(1-0)$ , and  $\text{C}^{18}\text{O}(1-0)$  lines ( $\nu_{^{12}\text{CO}(1-0)} = 115.271$  GHz,  $\nu_{^{13}\text{CO}(1-0)} = 110.201$  GHz, and  $\nu_{\text{C}^{18}\text{O}(1-0)} = 109.782$  GHz rest-frame frequencies, respectively) from individual star-forming galaxies to produce a statistically robust study for the content of these isotopologues up to  $z = 0.2$ .

This paper is structured as follows. In Section 2, we present the Atacama Large Millimetre/sub-millimetre Array (ALMA) data used in this work. Section 3 details the way we modelled the stacked  $^{12}\text{CO}$ ,  $^{13}\text{CO}$ , and  $\text{C}^{18}\text{O}$  fluxes as well as their errors. Section 4 presents the  $^{12}\text{CO}(1-0)/^{13}\text{CO}(1-0)$ , and  $^{13}\text{CO}(1-0)/\text{C}^{18}\text{O}(1-0)$  [hereafter,  $L'(^{12}\text{CO})/L'(^{13}\text{CO})$  and  $L'(^{13}\text{CO})/L'(\text{C}^{18}\text{O})$ ] line luminosity ratio measurements and their dependence as a function of global galaxy parameters, while Section 5 presents the discussion. Finally, our conclusions are shown in Section 6. Throughout this work, we assume a lambda cold dark matter cosmology adopting the values  $H_0 = 70 \text{ km s}^{-1} \text{ Mpc}^{-1}$ ,  $\Omega_{\text{M}} = 0.3$ , and  $\Omega_{\Lambda} = 0.7$  for the calculation of luminosity distances and physical scales.

## 2 DATA

### 2.1 Sample

In this work, we present  $^{13}\text{CO}(1-0)$  and  $\text{C}^{18}\text{O}(1-0)$  line measurements for 27 and 24 galaxies, respectively, which were previously detected by *Herschel* in [C II] (Ibar et al. 2015) and with ALMA in  $^{12}\text{CO}$  (Villanueva et al. 2017). The sample is part of the Valparaíso ALMA/APEX Line Emission Survey (VALES; Villanueva et al. 2017; Cheng et al. 2018) designed to characterize the CO emission line of low- $J$  transitions from typical star-forming and starburst galaxies up to  $z = 0.35$ . The parent population comes from dusty galaxies taken from the equatorial fields of the *Herschel* Astrophysical Terahertz Large Area Survey (Eales et al. 2010). Galaxies were selected using a spectroscopic redshift at  $0.02 < z < 0.2$ , and a *Herschel* detection near the peak of the spectral energy distribution (SED) of a normal star-forming galaxy ( $S_{160 \mu\text{m}} > 150 \mu\text{Jy}$ ). All galaxies have an unambiguous optical counterpart in the Sloan Digital Sky Survey (SDSS; Adelman-McCarthy et al. 2008), have high-quality spectra from the Galaxy and Mass Assembly survey (GAMA;<sup>1</sup> Liske et al. 2015; Driver et al. 2016;  $z_{\text{QUAL}} \geq 3$ ), and show a Petrosian SDSS radius smaller than 15 arcsec (see Ibar et al. 2015, for more details).

### 2.2 ALMA $^{13}\text{CO}(1-0)$ and $\text{C}^{18}\text{O}(1-0)$ observations

Observations with ALMA in band-3 were performed as part of project 2013.1.00530.S (P.I. E. Ibar), targeting the redshifted  $^{12}\text{CO}(1-0)$ ,  $^{13}\text{CO}(1-0)$ , and  $\text{C}^{18}\text{O}(1-0)$  emission lines for 27 VALES

<sup>1</sup><http://www.gama-survey.org/>

**Table 1.** New ALMA  $^{13}\text{CO}(1-0)$  and  $\text{C}^{18}\text{O}(1-0)$  observations (Project ID: 2013.1.00530.S) presented in this work. ‘PWV’ is the average PWV estimate for the observations. All data were taken using 32 12-m ALMA antennas. One observation taken on 2015 January 24 failed to run through the pipeline due to unknown reasons, so we have arbitrarily removed it from this work. Note that  $^{12}\text{CO}(1-0)$  observations can be found in Villanueva et al. (2017).

Target names HATLAS	Observation date	Flux calibrator	Bandpass calibrator	Phase calibrator	PWV (mm)
J085340.7+013348, J085405.9+011130	2015 January 24 (1/3)	Ganymede	J1058+0133	J0909+0121	5.9
J085356.4+001255, J083601.5+002617	–	–	–	–	–
J085112.9+010342, J090949.6+014847	2015 January 24 (2/3)	–	–	–	5.2
J085450.2+021208, J091205.8+002655	–	–	–	–	–
J085346.4+001252, J084428.4+020350	2015 January 24 (3/3)	–	–	–	4.5
J090005.0+000446, J090532.6+020222	–	–	–	–	–
J085111.4+013006, J083745.1–005141,	2015 January 25	–	–	–	4.5
J085828.6+003813, J085233.9+013422	–	–	–	–	–
J084350.8+005534, J083831.8+000044	2015 January 23 (1/2)	J0750+125	J0909+0121	J0901–0037	3.8
J084305.1+010855, J084907.1–005138	–	–	–	–	–
J084217.9+021223, J084139.6+015346	2015 January 23 (2/2)	–	–	–	3.9
J085748.0+004641, J084428.4+020657	–	–	–	–	–
J090750.0+010141, J085836.0+013149	2015 January 23	J0854+201	J0750+1231	J0901–0121	3.8
J084630.9+005055	–	–	–	–	–

galaxies. The  $^{12}\text{CO}(1-0)$  observations reached a root mean square (rms) of  $2 \text{ mJy beam}^{-1}$  at a spectral resolution of  $30 \text{ km s}^{-1}$  and are presented in Villanueva et al. (2017). The simultaneous  $^{13}\text{CO}(1-0)$  and  $\text{C}^{18}\text{O}(1-0)$  observations were taken between 2015 January 23 and 25, in compact configuration (maximum baseline of  $\sim 300 \text{ m}$ ) with precipitable water vapour (PWV) conditions in the range  $\sim 4$ – $6 \text{ mm}$ . The observational strategy consisted of grouping sources in terms of redshift, such that we could observe all 27 galaxies using just three spectral set-ups (each one using four spectral windows to cover  $7.5 \text{ GHz}$  of bandwidth). The grouped sources are shown in Table 1, including the different executions performed by ALMA to reach the requested sensitivity. Unfortunately, the spectral set-up missed  $\text{C}^{18}\text{O}(1-0)$  coverage in three galaxies.

Data reduction and imaging were performed using the same procedure as in Villanueva et al. (2017), where we developed a common pipeline within the Common Astronomy Software Applications (CASA version 4.4.0) to process all of the science goals. Each source was imaged with the TCLEAN task using a natural weighting. This yielded a restoring beam between 3 and 4 arcsec; nevertheless, for the purposes of this work, we fixed the restoring beam to a common value, at  $4''.5$ , for all sources. The  $^{13}\text{CO}(1-0)$  and  $\text{C}^{18}\text{O}(1-0)$  observations reached an rms noise of  $0.9 \text{ mJy beam}^{-1}$  at  $30 \text{ km s}^{-1}$  channel width ( $\sim 2 \times$  deeper than  $^{12}\text{CO}$  observations). We note that  $\sim 110 \text{ GHz}$  continuum emission is undetected at  $5\sigma$  significance in all sources down to an rms noise of  $4 \mu\text{Jy beam}^{-1}$ .

### 3 ANALYSIS

Out of the 27 galaxies, 26 have been previously spectrally detected at  $>5\sigma$  significance (signal-to-noise ratio, SNR) in  $^{12}\text{CO}(1-0)$  (Villanueva et al. 2017). The  $^{13}\text{CO}$  line was visually inspected for any individual detection. There were no confident  $^{13}\text{CO}(1-0)$  emission lines from individual spectra for any of the 27 galaxies. Nevertheless, using the information of the  $^{12}\text{CO}$  line widths as priors, we created moment-0 maps by collapsing the cube around  $\pm 1 \times \text{FWHM}_{^{12}\text{CO}}$  (full width at half-maximum) of the expected  $^{13}\text{CO}$  frequencies. In the collapsed images, we identify seven galaxies with  $\text{SNR} > 5$ . The remaining 21 galaxies have not been detected above a  $5\sigma$  significance in their moment-zero maps. Table 2 shows the SNRs, velocity-

**Table 2.**  $^{13}\text{CO}(1-0)$  detections from collapsed spectral images using  $\pm \text{FWHM}$   $^{12}\text{CO km s}^{-1}$  line width around  $^{13}\text{CO}(1-0)$  expected frequencies. (Col. 1) ID taken from Villanueva et al. (2017), (col. 2) observed SNR in moment-0 maps, (col. 3) velocity-integrated line flux densities with error measurements, and (col. 4)  $^{13}\text{CO}(1-0)$  luminosity with error measurements.

ID HATLAS	$\text{SNR}_{^{13}\text{CO}}$	$S_{^{13}\text{CO}} \Delta v$ $\text{mJy km s}^{-1}$	$L'_{^{13}\text{CO}}$ $\text{K km s}^{-1} \text{ pc}^2$
J090949.6+014847	5.6	$490 \pm 90$	$68.0 \pm 12.1$
J085346.4+001252	5.7	$225 \pm 40$	$2.9 \pm 0.5$
J084139.6+015346	6.1	$206 \pm 33$	$5.4 \pm 0.9$
J084350.8+005534	6.2	$458 \pm 73$	$11.9 \pm 2.0$
J083831.8+000044	6.4	$147 \pm 22$	$4.3 \pm 0.7$
J085748.0+004641	5.9	$343 \pm 58$	$8.9 \pm 1.5$
J090633.6+001526	7.0	$710 \pm 100$	$9.6 \pm 1.4$

integrated line flux densities, and luminosities of these individual  $^{13}\text{CO}$  detections. With respect to the  $\text{C}^{18}\text{O}$  emission line, we do not identify any detection in the spectra nor in the individual moment-0 maps using the same approach mentioned above.

Different techniques have been proposed to detect the emission of faint emission lines, falling below the detection limits. For example, Loomis et al. (2018) proposed a matched filtering method that uses a previously identified high signal-to-noise emission line as a kernel for filtering the uv signal and thereby facilitates the detection of any contiguous faint emission line. Similarly, Yen et al. (2016) proposed an image-plane line detection technique tailored to boost the SNR of faint emission lines in Keplerian discs. An independent approach has been the development of stacking techniques. This has been successful to detect the combined signal of faint emission coming from multiple objects of the same population over the electromagnetic spectrum, including the X-ray (Bartelmann & White 2003; Rodighiero et al. 2015; Yang et al. 2018), UV (Berry et al. 2012; Rigby et al. 2018), infrared (Dole et al. 2006; Duivenvoorden et al. 2020), sub-mm (Webb et al. 2003; Knudsen et al. 2005; Ibar et al. 2013; Millard et al. 2020), and radio (Miller et al. 2013; Bera et al. 2018; Perger et al. 2019) regimes. Moreover, stacking techniques have proven to be a robust method for line and continuum detections of high-redshift galaxies (Lehmer et al. 2007; Schinnerer et al. 2007;



Scoville et al. 2007; Miller et al. 2008). In order to compute stacked line ratios, in this study we explore three different techniques: two of them in the image plane: (i) stacking all the moment-0 maps and (ii) stacking all the frequency channels of all sources following a channel-by-channel basis, and additionally by (iii) stacking the individual *uv*-plane average signals.

### 3.1 Image stacking

#### 3.1.1 2D-moment-0 stacking

Based on the previously detected  $^{12}\text{CO}$  line widths and intensity peaks, we collapsed the data sets to create moment-0 maps. For this, we measure  $^{12}\text{CO}$  line widths using  $20 \text{ km s}^{-1}$  channel for all galaxies. Using the IMMOMENTS CASA task, we collapse each galaxy cube to create moment-0 maps for all  $^{12}\text{CO}$ ,  $^{13}\text{CO}$ , and  $\text{C}^{18}\text{O}$  data sets, around  $(\pm 1 \times \text{FWHM}_{12\text{CO}})$  the  $^{12}\text{CO}$ ,  $^{13}\text{CO}$ , and  $\text{C}^{18}\text{O}$  expected frequencies. We visually inspected all of the 27 collapsed  $^{12}\text{CO}$  images to correct for any possible spatial offsets with respect to the intensity peak. Such offsets exist; optical and sub-mm observations trace the stellar and molecular gas content of galaxies, respectively, and thus the location of the peaks does not necessarily match. Given that the reference coordinates of our ALMA observations were obtained from optical images, we apply astrometric corrections to our  $^{12}\text{CO}$  intensity maps, in order to correct any discrepancy between optical and  $^{12}\text{CO}$  images. These corrections are on average of the order of  $\sim 1''.4$  in random directions (smaller than the synthesized beam of  $4''.5$ ). Finally, using a stacking code that we developed, these images were stacked to obtain final collapsed signals reaching rms values of  $108 \text{ mJy beam}^{-1} \text{ km s}^{-1}$  for the  $^{12}\text{CO}$  line and  $18 \text{ mJy beam}^{-1} \text{ km s}^{-1}$  for the  $^{13}\text{CO}$  and  $\text{C}^{18}\text{O}$  emission lines. We note that these stacked values are  $\sim 5$  times deeper than individual moment-0 images.

To extract velocity-integrated line flux densities from the stacked signals, we create  $30 \text{ arcsec} \times 30 \text{ arcsec}$  stamps and model the sources with a 2D Gaussian profile, assuming that the stacked signals are point-like with an FWHM of  $4''.5$ .

#### 3.1.2 3D-image stacking

In this approach, for processing the data cubes, we consider a common spectral channel width for  $^{12}\text{CO}$ ,  $^{13}\text{CO}$ , and  $\text{C}^{18}\text{O}$  emission lines. To determine the best common spectral channel width to use, we kept in mind the idea of optimizing the SNR of the final stacked data cubes detections of both lines. For this, data cubes for all of the 27 galaxies were created using the CASA task TCLEAN assuming different velocity bin widths:  $[20, 40, 50, 80, 100, 125, 160, 200, 250, 400, 500, 800] \text{ km s}^{-1}$ . After this, we obtained a 3D stacked cube by combining the individual galaxy cubes following a channel-by-channel and pixel-by-pixel basis. We then obtained the SNR by measuring the peak at the central image pixel and central velocity channel ( $0 \text{ km s}^{-1}$ ). We measured the noise in the image excluding the central region. Peak flux densities were recorded for both the mean and median stacked cubes with different velocity width bins and for  $^{12}\text{CO}$ ,  $^{13}\text{CO}$ , and  $\text{C}^{18}\text{O}$  data sets. Fig. 1 shows this central channel SNR as a function of channel velocity width. We find that the  $^{12}\text{CO}$  signal maximizes at a channel width of  $200 \text{ km s}^{-1}$  for both the median (SNR $\sim 105.7$ ) and mean (SNR $\sim 96.6$ ). The stacked  $^{13}\text{CO}$  line maximizes at  $125 \text{ km s}^{-1}$  (SNR $\sim 8.0$ ) and  $500 \text{ km s}^{-1}$  (SNR $\sim 10.1$ ) for the median and mean, respectively. Finally, the  $\text{C}^{18}\text{O}$  line maximizes at  $125 \text{ km s}^{-1}$  for both the median (SNR $\sim 4.7$ ) and mean (SNR $\sim 5.5$ ) stacks. Based on these results, we decided to

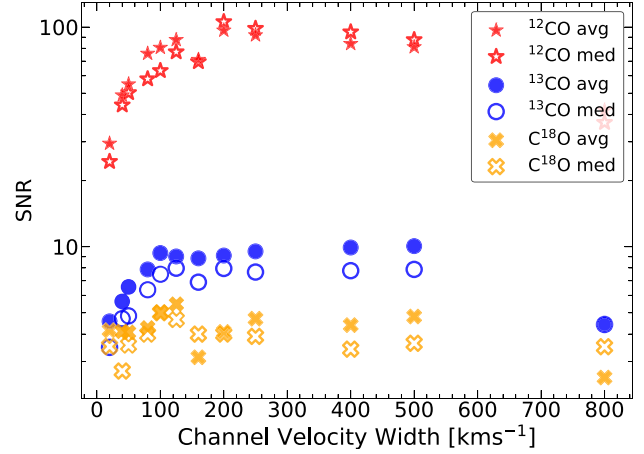


**Figure 1.** Stacked SNRs obtained from  $^{12}\text{CO}$  (stars),  $^{13}\text{CO}$  (circles), and  $\text{C}^{18}\text{O}$  (crosses) using different velocity channel widths, from 20 to  $800 \text{ km s}^{-1}$ . Filled symbols correspond to average SNR values while empty symbols correspond to median SNR values. These measurements are used to identify the best spectral channel width for 3D stacking (see Section 3.1.2).

use a common spectral channel width of  $125 \text{ km s}^{-1}$  for  $^{12}\text{CO}$ ,  $^{13}\text{CO}$ , and  $\text{C}^{18}\text{O}$  to image all data cubes in order to optimize the SNR in the final stacked images. We note that the same astrometric offsets used for moment-0 stacking, and described in Section 3.1.1, have been applied here, while velocity offsets based on the peak observed in  $^{12}\text{CO}$  are applied to all of the independent cubes in order to re-centre the signal. These offsets originate from small differences between the optical and sub-mm redshifts that trace different phases of the ISM.

Using a common channel width of  $125 \text{ km s}^{-1}$ , a spectral coverage of  $\pm 2000 \text{ km s}^{-1}$ , and a restoring beam with an FWHM of  $4''.5$ , we created the individual data cubes that are then stacked to get a cube containing the average  $^{12}\text{CO}$ ,  $^{13}\text{CO}$ , and  $\text{C}^{18}\text{O}$  signals. In order to measure velocity-integrated line flux densities, we first created spectral line profiles using a fixed aperture of  $15 \text{ arcsec}$  radius ( $\gtrsim 3 \times$  synthesized beam), centred at the source position. Thereby, we fitted a 1D Gaussian profile to obtain the global stacked velocity line width  $\text{FWHM}_f$  (see Fig. 2 lower panel). Hence, we took the central channel ( $0 \text{ km s}^{-1}$ , where the peak in the spectral line profile is located) to fit a 2D Gaussian profile assuming that the signal is point-like (see Fig. 2 upper right panel). Finally, the amplitude of the 2D Gaussian fit together with the line width is used to calculate velocity-integrated line flux densities.

#### 3.1.3 Systematic errors

In order to compute the systematic errors for our stacked velocity-integrated line flux density measurements, we ran Monte Carlo simulations using data cubes with the same physical scales (pixel size, synthesized beam, and primary beam) as those covered by the ALMA Band-3 observations.

We model each source as point-like (spatially) using a 2D circular Gaussian profile and spectrally by a 1D Gaussian profile centred at  $0 \text{ km s}^{-1}$ . We simulate a spectral coverage of  $\pm 2000 \text{ km s}^{-1}$ . These sources are added to a random, normally distributed background noise that has been convolved to the scale of the synthesized beam.

To simulate the stacking, we take 27 data cubes with sources at fixed signal-to-noise ratios ( $<\text{SNR}_{\text{in}}>$ ) and fixed velocity line widths. We stacked them and compute the velocity-integrated line

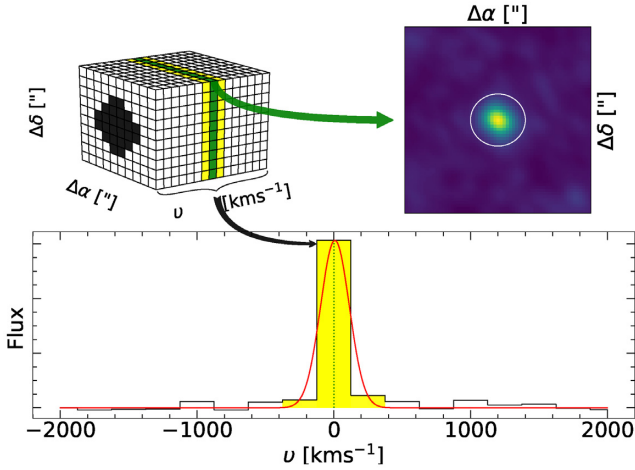


**Figure 2.** Velocity-integrated flux density measurements on a 3D stacked data cube. Upper left panel: 3D stacked image cube showing the central channel (green) at which the peak of the line is located, the channels covered by the fit  $\text{FWHM}_f$  line width highlighted in yellow, and the 15 arcsec radius aperture (black) used to generate the spectral line profile shown below. The bottom panel shows the spectral line profile (solid black line) and shows the 1D Gaussian fit (red line) to obtain the stacked velocity line width  $\text{FWHM}_f$  highlighted in yellow. The upper right panel shows the central channel where a 2D Gaussian profile is fitted (white) to obtain the amplitude of source. Both line width and amplitude are used to compute the velocity-integrated line flux densities.

flux densities as described in Sections 3.1.1 and 3.1.2. We repeat this process 1000 times, where amplitudes and velocity widths are simulated to take fixed values between 0 and 100 times the rms and line FWHMs between 50 and 500  $\text{km s}^{-1}$ , respectively. The extracted velocity-integrated line flux densities ( $S_{\text{out}}$ ) are measured and compared to the input values. Fig. 3 shows the  $\langle S_{\text{in}} \rangle / S_{\text{out}}$  ratio of 1000 simulated stacked data cubes for both, 2D-moment-0 (open stars) and 3D-image (open circles) stacking methods, and the average binned  $\langle S_{\text{in}} \rangle / S_{\text{out}}$  ratios (filled symbols) as a function of  $\text{SNR}_{\text{out}}$  of the composite stack images in the range between zero and 520 ( $=100 \times \sqrt{27}$ ). We note that the stacked images have  $\text{SNR}_{\text{out}}$  that are  $\sim \sqrt{27}$  times larger than the average  $\langle \text{SNR}_{\text{in}} \rangle$  of the individual images given by Poisson factor gained by the stacking approach. For example, if the  $^{13}\text{CO}$  stack has a measured  $\text{SNR}_{\text{out}} \sim 9$ , then this is produced by individual data cubes with an average  $\langle \text{SNR}_{\text{in}} \rangle \sim 1.73$ . Fig. 3 shows vertical lines indicating three different SNRs values  $\sim 6$ ,  $\sim 13$ , and  $\sim 18$  at which our 3D stacks show systematic errors of 8, 3, and 2 per cent while 2D-moment-0 stacks show 5, 3, and 1 per cent. These results show how typically 2D stacks show smaller systematic errors than 3D stacks. These differences tend to become negligible at  $\text{SNR}_{\text{out}} > 15$ .

### 3.2 uv stacking

Interferometric telescopes provide data that sample the brightness distribution of an observed source in Fourier space, where a point measurement per integration time is provided by a pair of antennas. The location of every point (visibility) in the Fourier space ( $uv$  plane) is determined by the separation of a pair of antennas as they trace the track of the source in the Fourier space during integration. The imaging process considers a deconvolution that assumes interpolations made on the  $uv$  plane that could lead to artefacts in the extracted images due to the intrinsic non-continuous sampling nature of interferometric data sets (Condon & Ransom 2016). Interferometric stacking analyses are usually performed using these

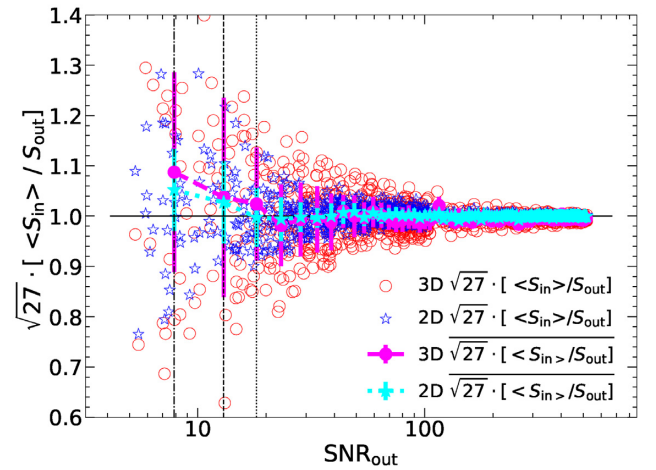


**Figure 3.** Simulated accuracy of the velocity-integrated flux density measurements ( $\langle S_{\text{in}} \rangle / S_{\text{out}}$ ) after stacking 27 galaxies. Stacked detections with high  $\text{SNR}_{\text{out}}$  have clearly better accuracy for the velocity-integrated flux density measurements.  $\langle S_{\text{in}} \rangle$  refers to the average velocity-integrated flux densities of the simulated sources used for the stacks, while  $S_{\text{out}}$  refers to the measured velocity-integrated flux density on the composite stacked images. 3D stacks are shown as open circles, 2D moment-0 stacks are shown as open stars, and filled symbols indicate the average  $\langle S_{\text{in}} \rangle / S_{\text{out}}$  binned by  $\text{SNR}_{\text{out}}$ . Vertical lines indicate the location of our  $^{12}\text{CO}$ ,  $^{13}\text{CO}$ , and  $\text{C}^{18}\text{O}$   $\text{SNR}_{\text{out}}$  stacked detections at  $\sim 6$  (dashed-dotted),  $\sim 13$  (dashed), and  $\sim 18$  (dotted) where 3D-image stacks show systematic errors of 8, 3, and 2 per cent while 2D-moment-0 stacks show 5, 3, and 1 per cent, respectively.

reconstructed images. Lindroos et al. (2015) developed *stacker*,<sup>2</sup> a tool that directly stacks interferometric continuum data sets in the  $uv$ -plane providing typical SNRs that are 20 per cent higher compared with continuum image stacking. *Stacker* was designed to perform the stacking analysis for continuum  $uv$  data; therefore, we mimic continuum maps as the average single channel maps of the  $^{12}\text{CO}$ ,  $^{13}\text{CO}$ , and  $\text{C}^{18}\text{O}$  emission line intensity data of the galaxies. To create individual single channel maps, we use the CASA task SPLIT to obtain an average  $uv$  data of the channels around the  $^{12}\text{CO}$  line observed frequency ( $\pm 1 \times \text{FWHM}_{12\text{CO}}$ ). As described in Section 3.1.1,  $^{12}\text{CO}$  line widths were measured using a 20  $\text{km s}^{-1}$  resolution, and these widths were also used to create the individual single channel maps for the  $^{13}\text{CO}$  and  $\text{C}^{18}\text{O}$  data sets. Similarly to previous approaches, we note that we have applied the same astrometric offset corrections to generate the single channel  $uv$  maps. To measure velocity-integrated line flux densities from the  $uv$  stacks, we create images using the CASA task TCLEAN following a similar approach as the images used for 2D- and 3D-image stacking procedures. Then as in 2D stacks, we model the sources with a 2D Gaussian profile and measured the velocity-integrated line flux densities from 30 arcsec  $\times$  30 arcsec stamps.

### 3.3 The differences between the stacking approaches

In this section, we discuss the stacking approaches described above in order to decide the most suitable one for our work. As mentioned before, each method is based on different assumptions; therefore, a direct comparison is not entirely trivial. For example, the images obtained from 2D stacking are generated using the CASA task IMMOMENTS that basically sums the intensities of the channels around  $\pm 1 \times \text{FWHM}_{12\text{CO}}$  for the  $^{12}\text{CO}$  observed frequency, while the  $^{13}\text{CO}$

<sup>2</sup><https://www.oso.nordic-alma.se/software-tools.php>

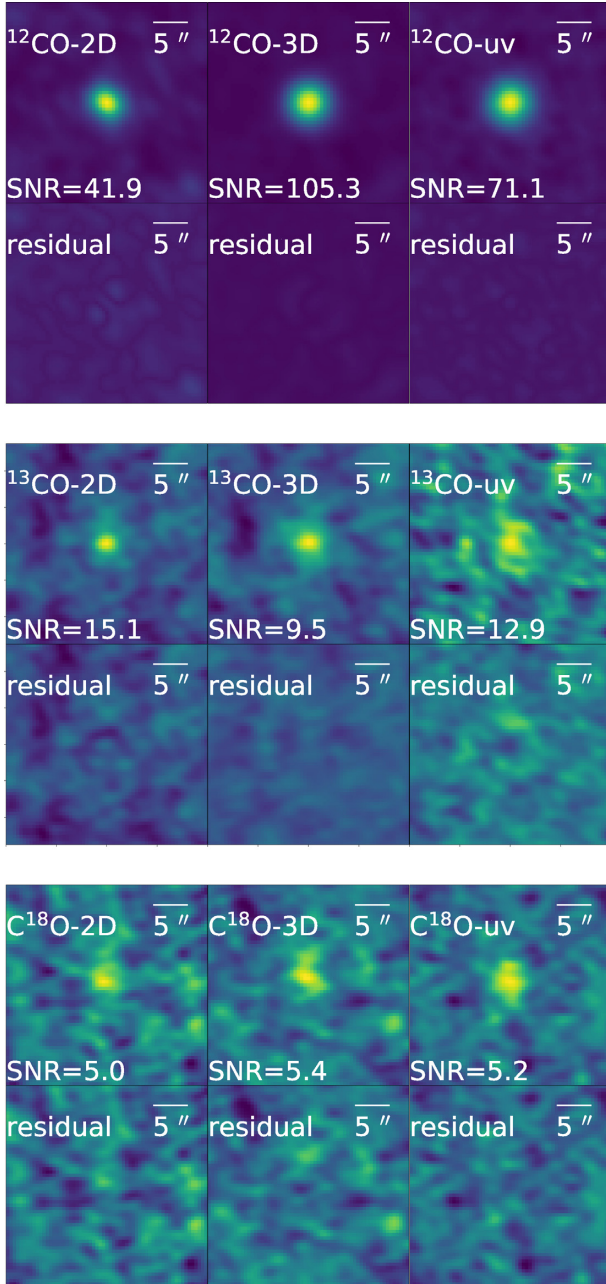


**Figure 4.** Final composite 30arcsec  $\times$  30arcsec stamps stacks (top) and residuals (bottom) from the corresponding flux modelling (see Section 3) for  $^{12}\text{CO}$  (upper panels),  $^{13}\text{CO}$  (middle panels), and  $\text{C}^{18}\text{O}$  (lower panels) emission lines from 2D-moment-0 stack (left column), 3D-image stack (middle column), and  $uv$  stack (right column).

and  $\text{C}^{18}\text{O}$  lines are blindly extracted at the expected frequencies using the derived  $^{12}\text{CO}$  redshifts. The 3D approach concentrates mainly on highlighting the intensities from the central channel of data cubes, where the velocity peak of the flux density profile is located. The case for the stacks obtained from a  $uv$  approach is constructed starting from the CASA task SPLIT that averages the  $uv$  intensities of the channels where the lines are located; these channels are exactly the same as those channels used to create the moment-0 maps for 2D stacking.

In Fig. 4, we show 30arcsec  $\times$  30arcsec image stacks and residuals after point-source extraction for the three methods explored in this work. All three different approaches result in similar

**Table 3.** SNR detection for  $^{12}\text{CO}$ ,  $^{13}\text{CO}$ , and  $\text{C}^{18}\text{O}$  stacked line emission, obtained from three different stacking methods explored in this work: (1) 2D-moment-0 stacking, (2) 3D-image stacking, and (3)  $uv$  stacking.

SNR	Moment-0	$uv$ stacking	3D stacking
$^{12}\text{CO}$	41.9	71.1	105.3
$^{13}\text{CO}$	15.1	12.9	9.5
$\text{C}^{18}\text{O}$	5.0	5.2	5.4

velocity-integrated line flux densities within the errors. However, we find that for a bright line like  $^{12}\text{CO}$   $uv$  stacks show an SNR  $\sim 1.6\times$  higher than that obtained from 2D stacking method (see Table 3). This result is similar to that found by Lindroos et al. (2015), who reported that continuum  $uv$  stacking SNR was up to 20 per cent higher than the continuum image stacking. Nevertheless, we find that for  $^{12}\text{CO}$  3D-image stacking shows to be the method with the highest SNR, being 2.5 and 1.6 times higher than 2D-moment-0 stacking and  $uv$  stacking SNRs, respectively. On the other hand, the 3D stacking method shows the lowest SNR for the faint lines like  $^{13}\text{CO}$ , while the 2D-moment-0 and  $uv$  stacking methods show similar SNRs. We note that, all the stacking methods applied on  $\text{C}^{18}\text{O}$  emission line show similar SNRs. Even though *stacker* was specially designed to stack  $uv$  continuum data sets and it has been successfully applied for  $uv$  emission line stacking (Fujimoto et al. 2018, 2019; Carvajal et al. 2020; Fudamoto et al. 2020) using a similar procedure as described here, this is the first time that  $uv$  and image stacking methods for emission line observations are directly compared. Driven by the previously available  $^{12}\text{CO}$  data presented in Villanueva et al. (2017), we decide to use the 2D (moment-0) approach to measure values, as this method yields the highest  $^{13}\text{CO}$  stacked SNRs that are straightforward to interpret and simple to calculate.

### 3.4 Luminosity measurements

We compute the  $^{12}\text{CO}$ ,  $^{13}\text{CO}$ , and  $\text{C}^{18}\text{O}$  luminosities using the velocity-integrated line flux densities following (Solomon & Vanden Bout 2005)

$$L'_{\text{CO}} = 3.25 \times 10^7 S \Delta \nu \nu_{\text{obs}}^{-2} D_L^2 (1+z)^{-3}, \quad (1)$$

where  $L'_{\text{CO}}$  is measured in  $\text{K km s}^{-1} \text{pc}^2$ ,  $S \Delta \nu$  is the velocity-integrated line flux density in units of  $\text{Jy km s}^{-1}$ ,  $\nu_{\text{obs}}$  is the observed frequency of the emission line in GHz,  $D_L$  is the luminosity distance in Mpc, and  $z$  is the redshift.

Considering the fact that we are analysing average properties from galaxies at different redshifts, special consideration should be taken to convert to intrinsic luminosities. To determine the dispersion of the stacked luminosity measurements, we have used a Monte Carlo simulation considering that the error from the velocity-integrated line flux density measurements is normally distributed, and at the same time assume a random sampling for the redshift distribution of the parent stacked sample. Repeating this simulation, we get a distribution of luminosities from which we can then infer the  $1\sigma$  confidence intervals (CI) of our average luminosity measurements. Since each galaxy population has a different redshift distribution, their CIs are independent from one population to another. We note that the differences between intensity and luminosity ratio measurements are negligible. The luminosity ratio of any pair of lines ( $L'_1, L'_2$ ) comes from converting their fluxes into luminosities following equation (1). Given that the redshifts ( $z_1, z_2$ ) for both lines are the same, the redshift and luminosity distance dependences



vanish leading to equation (2).

$$\frac{L'_1}{L'_2} = \frac{S_1 \Delta v_1 v_1^{-2} D_{L_1}^{-2} (1+z_1)^{-3}}{S_2 \Delta v_2 v_2^{-2} D_{L_2}^{-2} (1+z_2)^{-3}} = \frac{I_1 v_1^{-2}}{I_2 v_2^{-2}}. \quad (2)$$

In particular,  $L'(^{12}\text{CO})/L'(^{13}\text{CO}) = 0.91 \times I(^{12}\text{CO})/I(^{13}\text{CO})$  and  $L'(^{13}\text{CO})/L'(\text{C}^{18}\text{O}) = 0.99 \times I(^{13}\text{CO})/I(\text{C}^{18}\text{O})$ , which enable us to make direct comparisons between our results and different intensity and luminosity ratios available in the literature.

## 4 RESULTS

### 4.1 The $L'(^{12}\text{CO})/L'(^{13}\text{CO})$ ratio

The VALES survey provides a wide range of global galaxy properties such as stellar masses, SFRs, morphologies, luminosities, etc. In this section, we present the measured  $L'(^{12}\text{CO})/L'(^{13}\text{CO})$  luminosity ratios to search for possible dependences on different global galaxy parameters.

#### 4.1.1 Morphological and environmental dependence

A morphological and environmental dependence of the  $I(^{12}\text{CO})/I(^{13}\text{CO})$  line intensity ratio has been reported by previous studies. While merger systems show a higher  $I(^{12}\text{CO})/I(^{13}\text{CO})$  intensity ratio when compared with normal spiral galaxies (Casoli et al. 1992b; Taniguchi & Ohya 1998; Taniguchi, Ohya & Sanders 1999), galaxies in dense environments show a lower  $I(^{12}\text{CO})/I(^{13}\text{CO})$  intensity ratio (Alatalo et al. 2015). Initially, we explore the morphological and environmental classification available for our sample, according to the most prominent morphological features: bulge (B), disc (D), merger-irregular (M), and (C) that denotes if the source has multiple projected neighbouring systems ('companions'), as based on a visual inspection presented by Villanueva et al. (2017) to multiwavelength imaging from the GAMA survey.

We split our sample into five different subsets: (0) all galaxies ( $n = 27$ ; open symbols); (1) all galaxies excluding clear mergers (B, D, BC, DC;  $n = 24$ ); (2) bulge- and disc-dominated galaxies with projected companions (BC, DC;  $n = 8$ ); (3) bulge- and disc-dominated galaxies without any companion (B, D;  $n = 16$ ); and (4) mergers (M;  $n = 3$ ) (see Fig. 5).

In Table 4, we present the measured average  $L'(^{12}\text{CO})/L'(^{13}\text{CO})$  line luminosity ratio and average  $\langle\text{SFR}\rangle$ ,  $\langle\text{SFE}\rangle$ , and  $\langle L_{\text{IR}}\rangle$  values for the five different morphological galaxy populations explored in this work. Using all of the 27 galaxies, we find an average  $L'(^{12}\text{CO})/L'(^{13}\text{CO})$  line luminosity ratio of  $16.1 \pm 2.5$ . This value is in agreement with the values for mergers ( $12 \pm 3$ ) and interacting ETGs ( $15 \pm 5$ ) reported by Alatalo et al. (2015), and to the ratio of nearby spirals, starburst, and ETGs (excluding those belonging to the Virgo Cluster used by Alatalo et al. 2015) reported by Davis (2014) ( $12 \pm 1.0$ ). Mergers and galaxies with a visible companion tend to show higher  $L'(^{12}\text{CO})/L'(^{13}\text{CO})$  line luminosity ratios. In particular, mergers show the highest  $\langle\text{SFR}\rangle$ ,  $\langle\text{SFE}\rangle$ , and  $\langle L_{\text{IR}}\rangle$  average values among the different morphological classifications, and also show an  $L'(^{12}\text{CO})/L'(^{13}\text{CO})$  line luminosity ratio 2 times higher than that found in galaxies without a companion. These findings, however, are at low significance (mainly due to the low number statistics). Besides, these ratios are in good agreement with the ratios reported by Alatalo et al. (2015), who found that group galaxies present  $L'(^{12}\text{CO})/L'(^{13}\text{CO})$  line luminosity ratios 2 times higher than those of field galaxies.

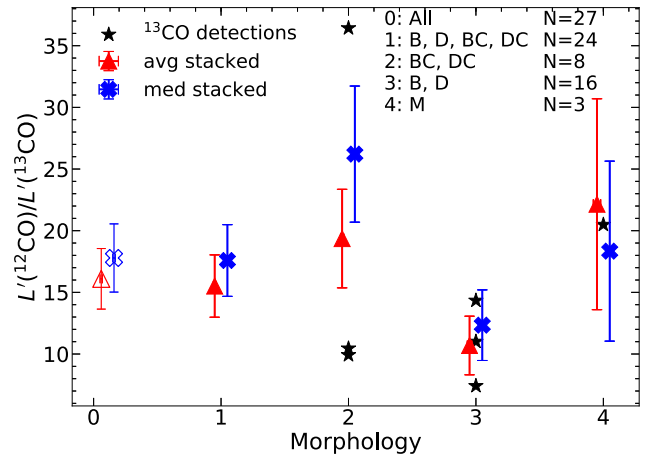


**Figure 5.** Average (red triangles) and median (blue crosses) stacked  $L'(^{12}\text{CO})/L'(^{13}\text{CO})$  line luminosity ratio values as a function of optical morphological properties as presented in Villanueva et al. (2017): (0) all galaxies ( $n = 27$ ), open symbols; (1) all galaxies excluding mergers (B, D, BC, DC;  $n = 24$ ); (2) bulge- and disc-dominated galaxies with projected companions (BC, DC;  $n = 8$ ); (3) bulge- and disc-dominated galaxies without any companion (B, D;  $n = 16$ ); and (4) mergers (M;  $n = 3$ ). Error bars correspond to  $1\sigma$  CIs for average ratios.

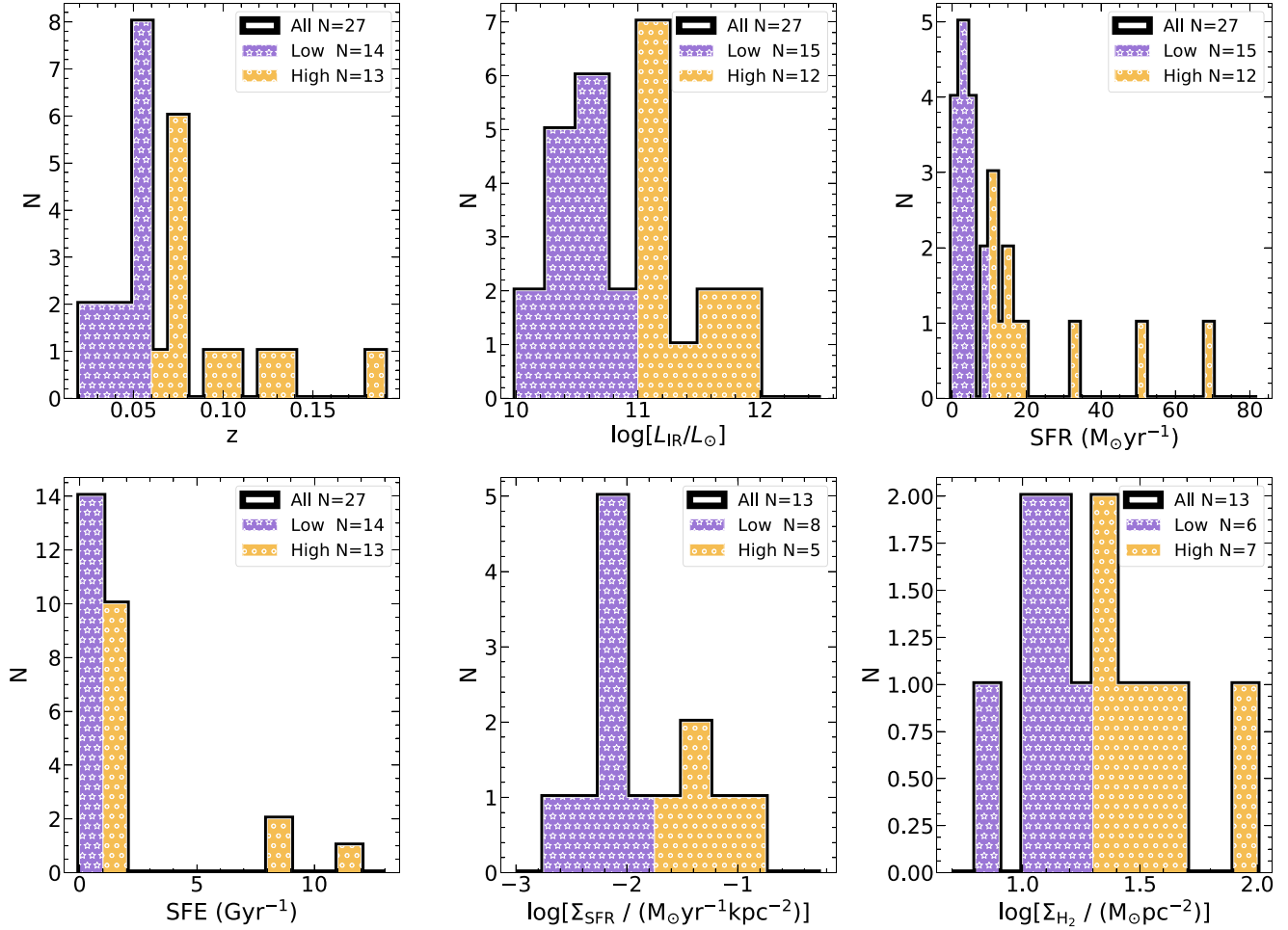
#### 4.1.2 The star formation activity

Villanueva et al. (2017) derived various global galaxy properties, including SFR, star formation efficiency (SFE), molecular gas surface density ( $\Sigma_{\text{H}_2}$ ), SFR surface density ( $\Sigma_{\text{SFR}}$ ), stellar mass ( $M_*$ ), gas depletion time ( $\tau$ ), and projected size ( $R_{\text{FWHM}}$ ). The total IR luminosity was obtained as described in Ibar et al. (2015) by integrating the best-fitting SED between 8 and 1000  $\mu\text{m}$  using photometry from IRAS, Wide-field Infrared Survey Explorer (WISE), and *Herschel*. The SFR was estimated following  $\text{SFR} (M_\odot \text{ yr}^{-1}) = 10^{-10} \times L_{\text{IR}}$  assuming a Chabrier (2003) IMF. The molecular gas mass was computed using  $L'_{\text{CO}}$  and assuming an  $\alpha_{\text{CO}}$  conversion factor dependent on the morphological classification ( $\alpha_{\text{CO}} = 4.6 \text{ K km s}^{-1} \text{ pc}^2$  for B- and D-dominated galaxies and  $\alpha_{\text{CO}} = 0.8 \text{ K km s}^{-1} \text{ pc}^2$  for mergers/interacting galaxies). The SFR and  $M_{\text{H}_2}$  surface densities were estimated by dividing the measured values by the area of a two-sided disc ( $2\pi R_{\text{FWHM}}^2$ ), where  $R_{\text{FWHM}}$  is the deconvolved FWHM along the semimajor axis obtained through fitting elliptical Gaussian profiles to the  $^{12}\text{CO}$  (1–0) moment-0 maps using the CASA task IMFIT. We consider the CO emission to be spatially resolved if the fitted semimajor axis is at least  $\sqrt{2}$  times larger than the semimajor axis of the synthesized beam. A more detailed discussion about the computations of these parameters can be found in Villanueva et al. (2017). With these in hand, we looked for possible dependences of  $L'(^{12}\text{CO})/L'(^{13}\text{CO})$  luminosity line ratio on these global galaxy properties by splitting our sample into two bins for each parameter. Fig. 6 shows the redshift,  $L_{\text{IR}}$ , SFR, SFE,  $\Sigma_{\text{SFR}}$ , and  $\Sigma_{\text{H}_2}$  distributions, split by low and high values. We find that the most significant trends for the  $L'(^{12}\text{CO})/L'(^{13}\text{CO})$  ratios are with  $L_{\text{IR}}$ , SFR, and SFE (see Figs 7 and 8). Table 5 shows the average  $L'(^{12}\text{CO})/L'(^{13}\text{CO})$  line luminosity ratios for low and high  $L_{\text{IR}}$ , SFR, SFE,  $\Sigma_{\text{SFR}}$ , and  $\Sigma_{\text{H}_2}$  populations.

Fig. 7 shows a trend of  $L'(^{12}\text{CO})/L'(^{13}\text{CO})$  line luminosity ratio with  $L_{\text{IR}}$  similar to that shown by Taniguchi & Ohya (1998), who used  $^{12}\text{CO}$  and  $^{13}\text{CO}$  line data taken from the literature for 61 nearby galaxies, including 8 luminous starburst galaxies. They found a correlation between  $L_{\text{FIR}}$  and  $L'(^{12}\text{CO})/L'(^{13}\text{CO})$  line

**Table 4.** Average  $L'(^{12}\text{CO})/L'(^{13}\text{CO})$  line luminosity ratio and average  $\langle\text{SFR}\rangle$ ,  $\langle\text{SFE}\rangle$ , and  $\langle L_{\text{IR}}\rangle$  values for different morphological classifications explored in this work (Villanueva et al. 2017; see Section 4.1.1 for more details).

ID	Group	$N$	$L'(^{12}\text{CO})/L'(^{13}\text{CO})$	$\langle\text{SFR}\rangle$ $\text{M}_{\odot} \text{ yr}^{-1}$	$\langle\text{SFE}\rangle$ $\text{Gyr}^{-1}$	$\langle\log[L_{\text{IR}}/L_{\odot}]\rangle$
0	All	27	$16.1 \pm 2.5$	$14.9 \pm 3.8$	$1.9 \pm 0.5$	$10.9 \pm 0.5$
1	BC, DC, B, D	24	$15.5 \pm 2.5$	$12.7 \pm 4.2$	$0.9 \pm 0.1$	$10.8 \pm 0.5$
2	BC, DC	16	$19.4 \pm 4.0$	$17.6 \pm 5.9$	$1.0 \pm 0.1$	$11.0 \pm 0.5$
3	B, D	8	$10.7 \pm 2.4$	$3.4 \pm 0.5$	$0.8 \pm 0.1$	$10.5 \pm 0.2$
4	M	3	$22.1 \pm 8.6$	$34 \pm 6.9$	$9.6 \pm 0.8$	$11.5 \pm 0.2$

**Figure 6.** Redshift,  $L_{\text{IR}}$ , SFR, SFE,  $\Sigma_{\text{SFR}}$ , and  $\Sigma_{\text{H}_2}$  distributions of the galaxies used in the  $^{12}\text{CO}$  and  $^{13}\text{CO}$  stacking analysis (solid black line), split by low (purple bars hatched with stars) and high (yellow bars hatched with circles) values.

ratio, where starburst galaxies with high infrared luminosities show higher  $[L'(^{12}\text{CO})/L'(^{13}\text{CO}) \geq 20]$  line ratios compared with normal galaxies. They dismissed physical gas properties such as density, temperature, or velocity gradients as responsible for the observed high  $L'(^{12}\text{CO})/L'(^{13}\text{CO})$  abundance ratio in starburst galaxies and conclude that the only possible mechanism behind the high  $^{12}\text{CO}/^{13}\text{CO}$  abundance ratio in starburst galaxies is an underabundance of  $^{13}\text{CO}$  with respect to  $^{12}\text{CO}$ . Our stacks (see Fig. 7) show a trend in which the high  $L_{\text{IR}}$  sample falls in the starburst region, while the low  $L_{\text{IR}}$  sample shows an average  $L'(^{12}\text{CO})/L'(^{13}\text{CO})$  line luminosity ratio similar to that found in normal galaxies.

To test the significance of the  $L'(^{12}\text{CO})/L'(^{13}\text{CO})-L_{\text{IR}}$  variations, we applied a Student's t-test to determine the probability that the  $L'(^{12}\text{CO})/L'(^{13}\text{CO})$  line luminosity ratio variations between the low- and high- $L_{\text{IR}}$  populations are not statistically significant. A large  $p$ -value indicates that the differences between the two sample means are not statistically significant, while a small one suggests that the differences between the two sample means are significant. Based on this test, we find that the differences in the  $L'(^{12}\text{CO})/L'(^{13}\text{CO})-L_{\text{IR}}$  variations are statistically significant (see Table 5). We then implemented a Spearman rank test to investigate a possible  $L'(^{12}\text{CO})/L'(^{13}\text{CO})-L_{\text{IR}}$  correlation, where  $p$ -values report



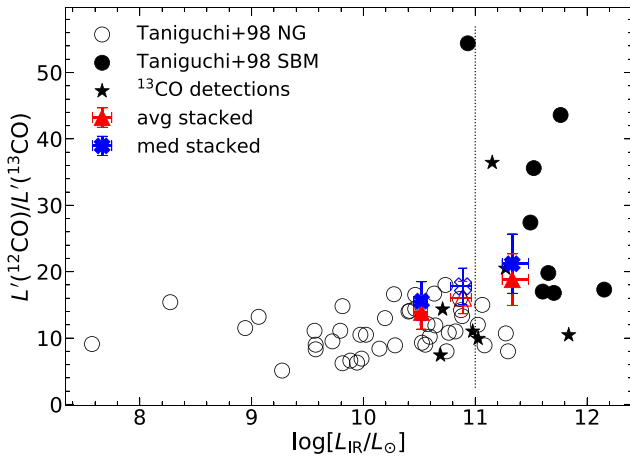


**Figure 7.** Average (red triangles) and median (blue crosses) stacked  $L'(^{12}\text{CO})/L'(^{13}\text{CO})$  line luminosity ratio for low- and high- $L_{\text{IR}}$  subsets (triangles). A dashed line indicates the boundary between low- and high- $L_{\text{IR}}$  populations. As reference, average and median line luminosity ratios considering all galaxies in open symbols are included. Error bars correspond to  $1\sigma$  CIs for average or median values based on Monte Carlo simulations. Individual  $^{13}\text{CO}$  detections (stars) and  $L'(^{12}\text{CO})/L'(^{13}\text{CO})$  line luminosity ratios of normal galaxies (NG open circles) and starburst mergers (SBM filled circles) scaled by a 1.75 factor to convert from far-IR to IR luminosities (see appendix E from Herrera-Camus et al. 2015) from Taniguchi & Ohyama (1998) are also included.

the probability of the lack of correlation between the two samples. A large  $p$ -value indicates that there is no significant correlation, while a small one suggests a significant correlation. The Spearman rank test was computed considering six galaxies (excluding HATLASJ090949.6 identified as an outlier; see Section 4.1.3) with individual  $^{13}\text{CO}$  detections, for which we could compute individual  $L'(^{12}\text{CO})/L'(^{13}\text{CO})$  luminosity ratios. The Spearman rank test does not provide evidence (see Table 6 first row) supporting a significant correlation between  $L'(^{12}\text{CO})/L'(^{13}\text{CO})$  and  $L_{\text{IR}}$ . This might be due to the reduced number (6) of galaxies with individual  $^{13}\text{CO}$  detections covering a small range of  $L_{\text{IR}}$ . However, if we also consider starburst galaxies and normal galaxies covering a wider range of  $L_{\text{FIR}}$  as reported by Taniguchi & Ohyama (1998), we find (see Table 6 second row) evidence supporting a moderate  $L'(^{12}\text{CO})/L'(^{13}\text{CO})$ – $L_{\text{IR}}$  correlation.

Fig. 8 (upper panels) shows  $L'(^{12}\text{CO})/L'(^{13}\text{CO})$  line luminosity ratio trends with SFR and SFE. Considering that SFRs are derived from far-IR luminosities, an expected trend in SFR is also identified (see Fig. 7). We also find that the higher the SFE ( $\text{SFR}/M_{\text{H}_2}$ ), the higher the  $L'(^{12}\text{CO})/L'(^{13}\text{CO})$  line luminosity ratio, following an expected similar trend as with SFR. By looking at the stacked signals, we find significant variations of the  $L'(^{12}\text{CO})/L'(^{13}\text{CO})$  line luminosity ratio when we split our sample by low and high SFR values (see Table 7). We notice that galaxies with high SFR not only show high  $L'(^{12}\text{CO})/L'(^{13}\text{CO})$  luminosity ratio, but also show relatively high reservoirs of molecular gas. Table 7 shows the average values of redshift, molecular gas mass ( $M_{\text{H}_2}$ ), molecular gas mass-to-stellar mass ratio ( $M_{\text{H}_2}/M_{\star}$ ), and molecular gas fraction [ $f_{\text{H}_2} = M_{\text{H}_2}/(M_{\text{H}_2} + M_{\star})$ ] for our galaxy sample after splitting it into low and high SFR values. To estimate the significance of the observed differences between the average properties ( $M_{\text{H}_2}$ ,  $M_{\text{H}_2}/M_{\star}$ ,  $f_{\text{H}_2}$ ) in the low- and high-SFR populations, we applied a Kolmogorov–Smirnov (KS) test to compute the probability that low and high ( $z$ ,

$M_{\text{H}_2}/M_{\star}$ ,  $M_{\text{H}_2}/M_{\star}$ , and  $f_{\text{H}_2}$ ) distributions were drawn from the same parent population. A large  $p$ -value indicates that the distributions are identical, while a small one suggests that the distributions are different. In all cases, we find evidence to reject the null hypothesis that the observed properties in the low- and high-SFR populations were drawn from the same parent population (see Table 7).

We perform a similar analysis to that described by Davis (2014) that reported a positive correlation of the  $I(^{12}\text{CO})/I(^{13}\text{CO})$  line intensity ratio with  $\Sigma_{\text{SFR}}$  and  $\Sigma_{\text{H}_2}$ . In our case, only 13 galaxies are known to be resolved in  $^{12}\text{CO}$ , enabling us to derive  $\Sigma_{\text{SFR}}$  and  $\Sigma_{\text{H}_2}$ . In Fig. 8 (lower panels), we show the  $L'(^{12}\text{CO})/L'(^{13}\text{CO})$  line luminosity ratio as a function of  $\Sigma_{\text{SFR}}$  split in high ( $10^{-2.1}$ – $10^{-1} \text{ M}_{\odot} \text{ yr}^{-1} \text{ kpc}^{-2}$ ) and low ( $10^{-2.6}$ – $10^{-2} \text{ M}_{\odot} \text{ yr}^{-1} \text{ kpc}^{-2}$ ) values. Individual  $^{13}\text{CO}$  galaxy detections from Davis (2014) are also overplotted. Concerning the dependences of  $L'(^{12}\text{CO})/L'(^{13}\text{CO})$  as a function of  $\Sigma_{\text{H}_2}$ , when we split by low ( $10^{0.8}$ – $10^{1.3} \text{ M}_{\odot} \text{ pc}^{-2}$ ) and high ( $10^{1.3}$ – $10^{-2} \text{ M}_{\odot} \text{ pc}^{-2}$ ) values, a moderate trend is found.

We applied a Student’s  $t$ -test to evaluate the probability that the null hypothesis [i.e. that the  $L'(^{12}\text{CO})/L'(^{13}\text{CO})$  line luminosity ratio variations between the low and high SFR, SFE,  $\Sigma_{\text{SFR}}$ , and  $\Sigma_{\text{H}_2}$  populations are not statistically significant] is true. We find supporting evidence that  $L'(^{12}\text{CO})/L'(^{13}\text{CO})$  variations between low and high SFR and SFE populations are statistically significant. On the other hand, we do not find evidence that supports that  $L'(^{12}\text{CO})/L'(^{13}\text{CO})$  variations between low and high  $\Sigma_{\text{SFR}}$  and  $\Sigma_{\text{H}_2}$  populations are not statistically significant (see Table 5). The lack of a significant difference of  $L'(^{12}\text{CO})/L'(^{13}\text{CO})$  with both  $\Sigma_{\text{SFR}}$  and  $\Sigma_{\text{H}_2}$  shown in the lower panels of Fig. 8 is most probably due to the reduced number of galaxies used for  $\Sigma_{\text{SFR}}$  and  $\Sigma_{\text{H}_2}$  stacks and the relatively small range of surface densities explored in this work. Finally, we note that we did not find any significant variations of  $L'(^{12}\text{CO})/L'(^{13}\text{CO})$  with redshift and stellar mass, as with  $\Sigma_{\text{H}_2}$ . This might be caused by the relatively small range of redshift [0.025–0.195] and stellar masses [ $\log(M/M_{\odot})=9.8$ –10.9] explored in this work.

#### 4.1.3 $^{13}\text{CO}$ individual detections

We have included the  $L'(^{12}\text{CO})/L'(^{13}\text{CO})$  line luminosity ratios of the individual  $^{13}\text{CO}$  detections (see Table 2) in Figs 5, 7, and 8. Galaxy J085748.0+004641 is classified as merger (M) while galaxy J083831.8+000044 is classified as a galaxy with a projected companion (DBC); they both show high  $L'(^{12}\text{CO})/L'(^{13}\text{CO})$  line luminosity ratios, in good agreement with previous findings. On the other hand, galaxies J085346.4+001252, J084139.6+015346, J084350.8+005534, and J090633.6+001526 are classified as galaxies that do not show any apparent projected companion and present low  $L'(^{12}\text{CO})/L'(^{13}\text{CO})$  line luminosity ratios, in agreement with those expected from galaxies with low  $L_{\text{IR}}$  values. Finally, galaxy J090949.6+014847 seems to be a peculiar galaxy showing a low  $L'(^{12}\text{CO})/L'(^{13}\text{CO})$  line luminosity ratio but with low SFE =  $1 \text{ Gyr}^{-1}$  and high  $L_{\text{IR}} = 10^{12} \text{ L}_{\odot}$  values. Thus, we identify J090949.6+014847 as an outlier and exclude it from the Spearman rank tests in the previous analyses. Stacking results are robust against the removal of this peculiar source from the sample.

#### 4.1.4 110.201 GHz stacked continuum emission

As discussed in Section 2.2, we do not detect continuum emission at  $\sim 110 \text{ GHz}$  above  $5\sigma$  significance down to an rms noise of  $4 \mu\text{Jy beam}^{-1}$  in any of the 27 galaxies of our sample. However, we could detect a high-signal-to-noise ratio ( $\text{SNR}=13$ ) emission

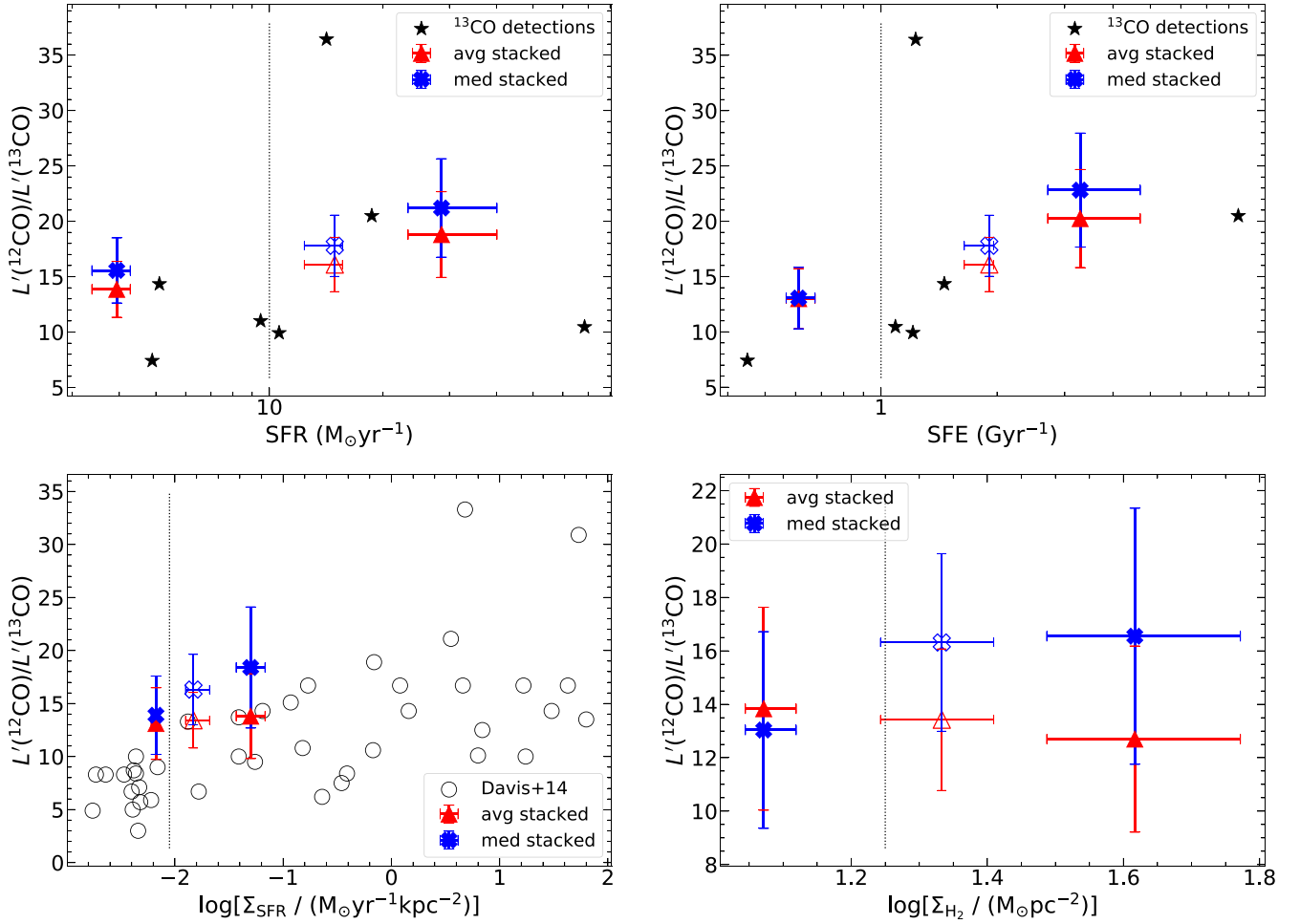


**Figure 8.** Average (red triangles) and median (blue crosses) stacked  $L'(^{12}\text{CO})/L'(^{13}\text{CO})$  line luminosity ratio for low and high SFR (upper left), SFE (upper right),  $\Sigma_{\text{SFR}}$  (lower left), and  $\Sigma_{\text{H}_2}$  (lower right) subsets (triangles). As reference, average and median line luminosity ratios considering all galaxies in open symbols and dashed lines indicating the boundary between low and high SFR, SFE,  $\Sigma_{\text{SFR}}$ , and  $\Sigma_{\text{H}_2}$  populations are included. Error bars correspond to  $1\sigma$  CIs for average or median values based on Monte Carlo simulations. Individual  $^{13}\text{CO}$  detections (stars) and  $L'(^{12}\text{CO})/L'(^{13}\text{CO})$  line intensity ratio of normal galaxies (open circles) from Davis (2014) are also included.

**Table 5.** Average  $L'(^{12}\text{CO})/L'(^{13}\text{CO})$  line luminosity ratio for our sample of galaxies split by high and low  $L_{\text{IR}}$ , SFR, SFE,  $\Sigma_{\text{SFR}}$ , and  $\Sigma_{\text{H}_2}$  values. Column 1: parameter of interest; column 2: range explored; column 3: the number of galaxies in the explored range; column 4: average value for parameter of interest; column 5: the average stacked  $L'(^{12}\text{CO})/L'(^{13}\text{CO})$  line luminosity ratio; columns 6 and 7: Student's t-test statistical reports ( $t$ ,  $p$ ) to assess the probability ( $p$ ) that the null hypothesis [ $L'(^{12}\text{CO})/L'(^{13}\text{CO})$  line luminosity ratio variations between the low- and high-SFR populations are not statistically significant] is true.

Parameter	Range	$N$	Average	$L'(^{12}\text{CO})/L'(^{13}\text{CO})$	t-test	
1	2	3	4	5	$t$	$p$
$\log[L_{\text{IR}}/L_{\odot}]$	[10.1–10.9]	14	$10.5 \pm 0.1$	$13.8 \pm 2.4$	−3.9	0.0006
	[11.0–11.9]	13	$11.3 \pm 0.1$	$18.7 \pm 3.9$	–	–
$\text{SFR } (\text{M}_{\odot} \text{ yr}^{-1})$	[1.8–9.5]	15	$3.9 \pm 0.6$	$13.3 \pm 2.4$	−4.3	0.0002
	[10.3–83.4]	12	$28.6 \pm 5.3$	$18.7 \pm 3.8$	–	–
$\text{SFE } (\text{Gyr}^{-1})$	[0.4–0.9]	14	$0.6 \pm 0.1$	$12.9 \pm 2.7$	−4.7	7E-05
	[1–11.7]	13	$3.3 \pm 0.6$	$19.4 \pm 4.2$	–	–
$\log[\Sigma_{\text{SFR}} / (\text{M}_{\odot} \text{ yr}^{-1} \text{ kpc}^{-2})]$	[−2.6 – −1]	13	$−1.8 \pm 0.1$	$12.5 \pm 2.4$	–	–
	[−2.6 – −2]	8	$−2.2 \pm 0.1$	$12.2 \pm 3.1$	−0.05	0.9
	[−2.1 – −1]	5	$−1.3 \pm 0.1$	$12.3 \pm 3.5$	–	–
$\log[\Sigma_{\text{H}_2} / (\text{M}_{\odot} \text{ pc}^{-2})]$	[0.8–2.0]	13	$1.3 \pm 0.1$	$12.5 \pm 2.5$	–	–
	[0.8–1.2]	6	$1.0 \pm 0.1$	$11.8 \pm 3.2$	−0.5	0.6
	[1.3–2.0]	7	$1.6 \pm 0.2$	$12.8 \pm 3.5$	–	–

**Table 6.** Spearman correlation test statistic ( $\rho$ ,  $p$ ), to assess the null hypothesis [no significant correlation between  $L'(^{12}\text{CO})/L'(^{13}\text{CO})$  and  $L_{\text{IR}}$ ] being true, for (1) 6 galaxies with  $^{13}\text{CO}$  individual detections for which we could compute individual  $L'(^{12}\text{CO})/L'(^{13}\text{CO})$  luminosity ratios and (2) 6 galaxies with  $^{13}\text{CO}$  individual detections plus 61 starburst and normal galaxies reported by Taniguchi & Ohyama (1998).

Sample	$N$	$\rho$	$p$
1) Galaxies with $^{13}\text{CO}$ detections	6	0.71	0.14
2) + Starburst and normal galaxies	67	0.55	4E-6

**Table 7.** Average values of various galaxy parameters (column 1): redshift, molecular gas mass ( $M_{\text{H}_2}$ ), molecular gas mass-to-stellar mass ratio ( $M_{\text{H}_2}/M_*$ ), and molecular gas fraction [ $f_{\text{H}_2} = M_{\text{H}_2}/(M_{\text{H}_2} + M_*)$ ] for the sample after splitting it into low (column 2) and high (columns 3) SFR values. Columns 4 and 5 contain the KS statistical reports ( $D$ ,  $p$ ) to assess the probability that low and high ( $z$ ,  $M_{\text{H}_2}/M_*$ , and  $f_{\text{H}_2}$ ) were drawn from populations with identical distributions.

Parameter	SFR ( $\text{M}_{\odot} \text{ yr}^{-1}$ )		KS	
	Low $N = 15$ [1.8–9.5]	High $N = 12$ [10.3–83.4]		
1	2	3	4	5
$\langle z \rangle$	$0.04 \pm 0.01$	$0.10 \pm 0.04$	0.8	0.0001
$\langle \log[M_{\text{H}_2}/\text{M}_{\odot}] \rangle$	$8.9 \pm 0.6$	$10.1 \pm 0.1$	0.5	0.03
$\langle M_{\text{H}_2}/M_* \rangle$	$0.17 \pm 0.04$	$0.53 \pm 0.18$	0.6	0.02
$\langle f_{\text{H}_2} \rangle$	$0.14 \pm 0.06$	$0.28 \pm 0.15$	0.55	0.02

**Table 8.**  $^{13}\text{CO}$  stacked continuum emission split by low- and high-SFR populations.

Parameter	SFR ( $\text{M}_{\odot} \text{ yr}^{-1}$ )		
	All $N = 27$	Low $N = 15$ [1.8–9.5]	High $N = 12$ [10.3–83.4]
SNR	13	6	15
$\text{S}_{13\text{CO}} \Delta\nu [\mu\text{Jy km s}^{-1}]$	$82 \pm 6$	$64 \pm 10$	$110 \pm 7$

after stacking the individual continuum emission of our 27 galaxy sample coming from the  $^{13}\text{CO}$  data sets. As with the  $^{12}\text{CO}$ ,  $^{13}\text{CO}$ , and  $\text{C}^{18}\text{O}$  stacks, we split our sample by low- and high-SFR populations (see Table 8). Similar to what we found for the  $L'(^{12}\text{CO})/L'(^{13}\text{CO})$  ratio, galaxies with higher SFR show the higher continuum emission compared with galaxies with low SFR. The detected continuum emission does not show any discrepancy with the expected average continuum emission at  $\sim 110$  GHz extrapolated from the SEDs presented in Villanueva et al. (2017). However, further analyses (beyond the scope of this paper) at these frequencies are needed to uncover the origin of the continuum emission (*e.g. free-free, dust, and ionized gas emission*) contributing to the SEDs of these galaxies and its relation with their star formation activity.

#### 4.2 $L'(^{13}\text{CO})/L'(\text{C}^{18}\text{O})$ correlations

Our ALMA Band-3 observations helped with the exploration of the  $\text{C}^{18}\text{O}(1-0)$  emission line for 24 VALES galaxies. Following a similar approach as before, in this section we only use these 24 galaxies with simultaneous  $\text{C}^{18}\text{O}$ ,  $^{13}\text{CO}$ , and  $^{12}\text{CO}$  observations. Figs 9 and 10 show the trends for  $L'(^{12}\text{CO})/L'(^{13}\text{CO})$  and  $L'(^{13}\text{CO})/L'(\text{C}^{18}\text{O})$  as a function of  $L_{\text{IR}}$ , SFR, and SFE, respectively, and Table 9

for average  $L'(^{12}\text{CO})/L'(^{13}\text{CO})$  and  $L'(^{13}\text{CO})/L'(\text{C}^{18}\text{O})$  values. The average  $L'(^{13}\text{CO})/L'(\text{C}^{18}\text{O})$  line luminosity ratio found is  $2.5 \pm 0.6$ , which is in good agreement with the  $I(^{13}\text{CO})/I(\text{C}^{18}\text{O})$  line intensity ratio found for starburst galaxies ( $3.4 \pm 0.9$ ) but slightly lower than the average ratio found in nearby normal spiral galaxies ( $6.0 \pm 0.9$ ) reported by Jiménez-Donaire et al. (2017). The central panel of Fig. 10 shows the  $L'(^{13}\text{CO})/L'(\text{C}^{18}\text{O})$  line luminosity ratio as a function of SFR (see Table 10) and also includes values reported in the literature gathered by Romano et al. (2017) and split by normal, starbursts, and ULIRGs.

As with  $L'(^{12}\text{CO})/L'(^{13}\text{CO})$  trends discussed in Section 4.1, we implemented a Student's t-test to evaluate the significance of the  $L'(^{12}\text{CO})/L'(^{13}\text{CO})$  and  $L'(^{13}\text{CO})/L'(\text{C}^{18}\text{O})$  variations with  $L_{\text{IR}}$ , SFR, and SFE considering the 24 galaxies with  $\text{C}^{18}\text{O}$  coverage. We find that the differences found in the  $L'(^{12}\text{CO})/L'(^{13}\text{CO})$  and  $L'(^{13}\text{CO})/L'(\text{C}^{18}\text{O})$  variations between low and high  $L_{\text{IR}}$ , SFR, and SFE populations are statistically significant (see Table 9). We also applied a KS test to assess the probability that the null hypothesis (low and high SFR, SFE,  $L_{\text{IR}}$ ,  $M_{\text{H}_2}/\text{M}_{\odot}$ ,  $M_{\text{H}_2}/M_*$ , and  $f_{\text{H}_2}$  populations were drawn from the same parent population) is true, considering the reduced 24 galaxy sample with  $\text{C}^{18}\text{O}$  coverage. Table 10 shows the average values of redshift,  $M_{\text{H}_2}/\text{M}_{\odot}$ ,  $M_{\text{H}_2}/M_*$ , and  $f_{\text{H}_2}$  split by low and high SFR values and the KS statistics ( $D$ ,  $p$ ). We find supporting evidence to reject the null hypothesis that the low and high SFR populations were drawn from the same parent population. Therefore, galaxies with high  $L'(^{12}\text{CO})/L'(^{13}\text{CO})$  ratio (Fig. 9) and low  $L'(^{13}\text{CO})/L'(\text{C}^{18}\text{O})$  ratio (Fig. 10) also show relatively high  $L_{\text{IR}}$ , SFR, and SFE and high reservoirs of molecular gas (see Table 10). These line ratios can be explained by over-abundances of  $^{12}\text{CO}$  and  $\text{C}^{18}\text{O}$  (both produced in high-mass stars), with respect  $^{13}\text{CO}$ , that could be understood as a result of selective nucleosynthesis where high-mass stars enrich the ISM of these galaxies.

## 5 DISCUSSION

The  $L'(^{12}\text{CO})/L'(^{13}\text{CO})$  line luminosity ratios presented in this work can be affected by optical depth effects or by the different physical processes that have been invoked to explain large and low  $I(^{12}\text{CO})/I(^{13}\text{CO})$  line intensity ratios. The most relevant ones are: (i) selective photodissociation:  $^{12}\text{CO}$  molecules are more abundant than  $^{13}\text{CO}$  molecules and hence due to their higher density they are self-shielded against strong interstellar UV radiation fields, unlike less abundant  $^{13}\text{CO}$  molecules that are more easily photodissociated, leading to a  $^{13}\text{CO}$  underabundance and hence a higher  $I(^{12}\text{CO})/I(^{13}\text{CO})$  line intensity ratio in regions with strong UV radiation fields; (ii) chemical isotope-dependent fractionation, where gas kinetic temperatures elevate  $^{13}\text{CO}$  abundance through the isotopic charge exchange reaction (Watson 1977), where  $^{12}\text{CO} + ^{13}\text{C}^+ \rightarrow ^{12}\text{C}^+ + ^{13}\text{CO} + \Delta E$ ; and (iii) selective nucleosynthesis where massive stars in star-forming regions produce significantly higher amounts of  $^{12}\text{C}$  compared to  $^{13}\text{C}$  leading to a high  $I(^{12}\text{CO})/I(^{13}\text{CO})$  line intensity ratio (Henkel & Mauersberger 1993; Aalto et al. 1995).

The higher  $L'(^{12}\text{CO})/L'(^{13}\text{CO})$  line luminosity ratio found for galaxies with close companions may be explained by interaction activity. For example, during the early stages of a merger event, part of the gas escapes and disperses into the intergalactic medium (Mirabel & Sanders 1989). The remaining gas shrinks to the centre, becomes denser, and converted partially into molecular  $\text{H}_2$  gas. This fresh molecular gas with relatively low metallicity and hence a high



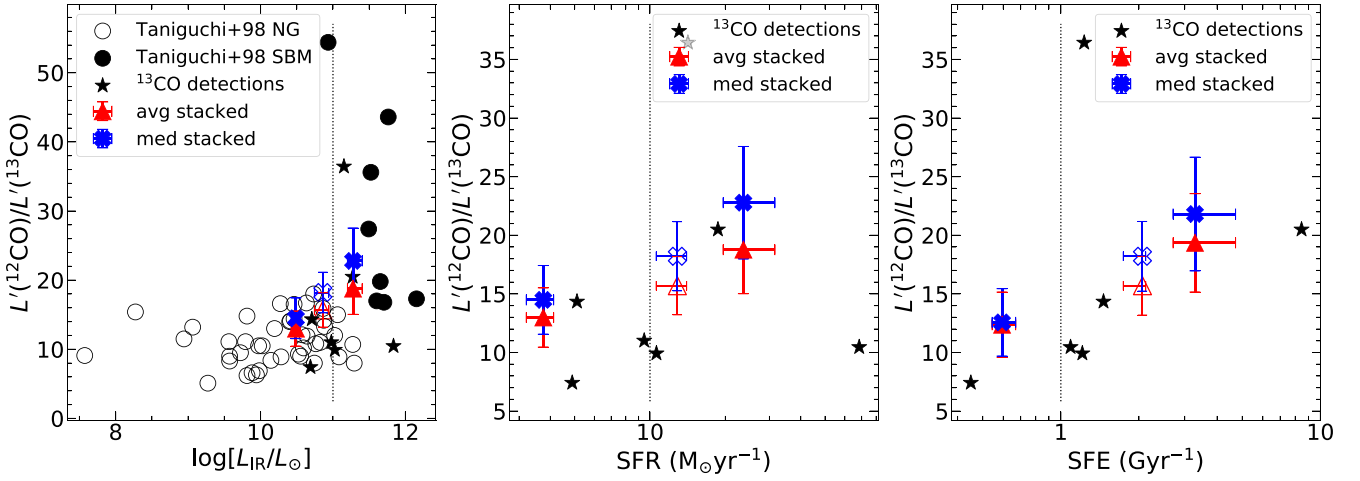


**Figure 9.** Average (red triangles) stacked  $L'(^{12}\text{CO})/L'(^{13}\text{CO})$  line luminosity ratio for low and high  $L_{\text{IR}}$  (left-hand panel), SFR (middle panel), and SFE (right-hand panel), subsets (triangles). As reference, average and median line luminosity ratios considering all galaxies in open symbols and dashed lines indicating the boundary between low and high  $L_{\text{IR}}$ , SFR, and SFE populations are included. Error bars correspond to  $1\sigma$  CIs for average (or median) values based on Monte Carlo simulations.  $L'(^{12}\text{CO})/L'(^{13}\text{CO})$  line ratios of normal galaxies (open circles) and starburst mergers (filled circles) scaled by a 1.75 factor to convert from far-IR to IR luminosities (see appendix E from Herrera-Camus et al. 2015). Data from Taniguchi & Ohya (1998) and individual  $^{13}\text{CO}$  detections (stars) are also included.

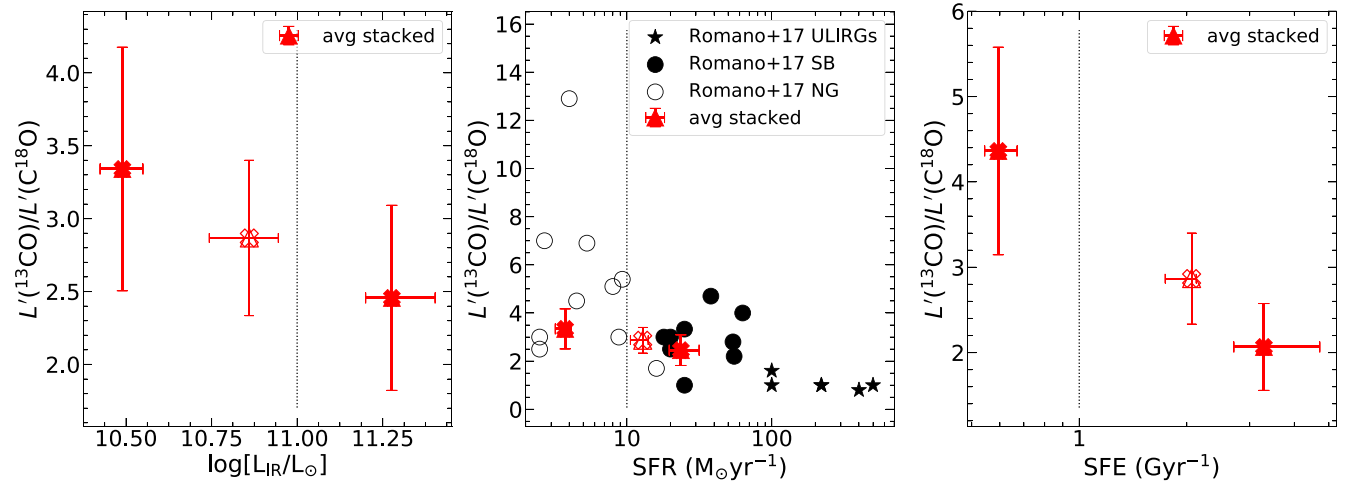


**Figure 10.** Average (red triangles) stacked  $L'(^{13}\text{CO})/L'(\text{C}^{18}\text{O})$  line luminosity ratio for low and high  $L_{\text{IR}}$  (left-hand panel), SFR (middle panel), and SFE (right-hand panel), subsets (triangles). As reference, average line luminosity ratios considering all 24 galaxies with  $\text{C}^{18}\text{O}$  coverage are shown in open symbols and dashed lines indicating the boundary between low and high  $L_{\text{IR}}$ , SFR, and SFE populations are included. Error bars correspond to  $1\sigma$  CIs for average values based on Monte Carlo simulations.  $L'(^{13}\text{CO})/L'(\text{C}^{18}\text{O})$  ratios reported in the literature and gathered by Romano et al. (2017) split by normal galaxies (NG open circles), starburst galaxies (SB filled circles), and ULIRGs (stars) as a function of SFR are also included. We note that median  $L'(^{13}\text{CO})/L'(\text{C}^{18}\text{O})$  line luminosity stacks are not included in our analyses due to low significance in these values.

$^{12}\text{C}/^{13}\text{C}$  luminosity ratio will trigger new starburst events boosting the  $^{12}\text{CO}/^{13}\text{CO}$  abundance ratio (Langer & Penzias 1990; Casoli et al. 1992b). On the other hand, the opposite scenario occurs in galaxies in denser environments, like galaxy clusters, where a deficit in  $^{12}\text{CO}$  is linked to the low  $I(^{12}\text{CO})/I(^{13}\text{CO})$  line ratios observed. Galaxies in clusters have lived long enough to enrich the ISM with  $^{13}\text{C}$  atoms from low-mass stellar nucleosynthesis, while at the same time, the evaporation or stripping of low-density GMCs as galaxies enter into the cluster moving through the ICM possibly reduces the presence of new starburst events and therefore would lead to a reduced  $I(^{12}\text{CO})/I(^{13}\text{CO})$  intensity ratio (Alatalo et al. 2015). In summary, the enhanced  $L'(^{12}\text{CO})/L'(^{13}\text{CO})$  line luminosity ratios observed in galaxy mergers (M) and galaxies with a projected companion

(BC, DC) that got relatively high SFR ( $34 \pm 6.9$  and  $17.6 \pm 5.9$ , respectively) could be explained by a new starburst activity in these systems. Galaxies without any projected companion (B, D) with low SFRs present a relatively low  $L'(^{12}\text{CO})/L'(^{13}\text{CO}) = 3.4 \pm 0.5$  line luminosity ratio, which could be explained by  $^{13}\text{C}$  enrichment of their ISM induced by low- and intermediate-mass stars in the absence of young starburst events.

The trends of  $L'(^{12}\text{CO})/L'(^{13}\text{CO})$  with  $L_{\text{IR}}$ , SFR, and SFE (see Figs 7, 8, and 9) found in this work provide the evidence that galaxies with low SFR, SFE, and  $L_{\text{IR}}$  also show low  $L'(^{12}\text{CO})/L'(^{13}\text{CO})$  line luminosity ratios in agreement to the idea that normal star-forming galaxies have larger gas consumption times to enrich with  $^{13}\text{C}$  the ISM from low- and intermediate-mass stars. On the other hand, galax-

**Table 9.** Average  $L'(^{12}\text{CO})/L'(^{13}\text{CO})$  and  $L'(^{13}\text{CO})/L'(\text{C}^{18}\text{O})$  line luminosity ratios for the sample of 24 VALES galaxies with  $\text{C}^{18}\text{O}$  observations split by low and high  $L_{\text{IR}}$ , SFR, and SFE values (see Figs 9 and 10). Column 1: parameter of interest; column 2: range explored; column 3: the number of galaxies in the explored range; column 4: average value for parameter of interest; columns 5 and 8: the average stacked  $L'(^{12}\text{CO})/L'(^{13}\text{CO})$  and  $L'(^{13}\text{CO})/L'(\text{C}^{18}\text{O})$  line luminosity ratios, respectively. Finally, we provide the Student's  $t$ -test statistical reports ( $t$ ,  $p$ ) to assess the probability that the null hypothesis [ $L'(^{12}\text{CO})/L'(^{13}\text{CO})$  and  $L'(^{13}\text{CO})/L'(\text{C}^{18}\text{O})$  line luminosity ratio variations between low and high  $L_{\text{IR}}$ , SFR, and SFE populations are not statistically significant] is true, located in columns 6 and 9 ( $t$  coefficient) and columns 7 and 10 (probability  $p$ -value), respectively.

Parameter	Range	$N$	Average	$L'(^{12}\text{CO})/L'(^{13}\text{CO})$	t-test		$L'(^{13}\text{CO})/L'(\text{C}^{18}\text{O})$	t-test	
1	2	3	4	5	$t$ 6	$p$ 7	8	$t$ 9	$p$ 10
$\log[L_{\text{IR}}/L_{\odot}]$	[10.1–11.0]	13	$10.5 \pm 0.1$	$13.0 \pm 2.5$	−4.4	0.002	$3.3 \pm 0.8$	−2.8	0.01
	[11.1–11.8]	11	$11.3 \pm 0.1$	$18.8 \pm 3.7$	–	–	$2.5 \pm 0.6$	–	–
SFR ( $\text{M}_{\odot} \text{ yr}^{-1}$ )	[1.3–9.5]	13	$3.7 \pm 0.5$	$13.0 \pm 2.6$	−4.2	0.0003	$3.3 \pm 0.8$	−2.8	0.01
	[10.3–68.5]	11	$23.6 \pm 4.0$	$18.8 \pm 3.8$	–	–	$2.5 \pm 0.6$	–	–
SFE ( $\text{Gyr}^{-1}$ )	[0.4–0.9]	11	$0.6 \pm 0.1$	$12.4 \pm 2.8$	−4.8	7E-5	$4.4 \pm 1.2$	−5.9	5E-6
	[1.1–11.8]	13	$3.3 \pm 0.6$	$19.4 \pm 4.2$	–	–	$2.1 \pm 0.5$	–	–

**Table 10.** Average values of different parameters (column 1): redshift, molecular gas mass ( $M_{\text{H}_2}$ ), molecular gas mass-to-stellar mass ratio ( $M_{\text{H}_2}/M_{\star}$ ), and molecular gas fraction [ $f_{\text{H}_2} = M_{\text{H}_2}/(M_{\text{H}_2} + M_{\star})$ ] considering 24 galaxies with  $\text{C}^{18}\text{O}$  coverage split by low (column 2) and high SFR values (column 3). Columns 4 and 5 contain the KS statistical reports ( $D$ ,  $p$ ) to assess the probability that low and high ( $z$ ,  $M_{\text{H}_2}$ ,  $M_{\text{H}_2}/M_{\star}$ , and  $f_{\text{H}_2}$ ) populations were drawn from populations with identical distributions.

Parameter	SFR ( $\text{M}_{\odot} \text{ yr}^{-1}$ )		KS	
	Low $N = 15$ [1.3–9.5]	High $N = 12$ [10.3–68.5]	$D$	$p$
1	2	3	4	5
$\langle z \rangle$	$0.04 \pm 0.01$	$0.10 \pm 0.04$	0.8	7E-5
$\langle \log[M_{\text{H}_2}/\text{M}_{\odot}] \rangle$	$8.8 \pm 0.1$	$9.9 \pm 0.1$	0.8	0.01
$\langle M_{\text{H}_2}/M_{\star} \rangle$	$0.15 \pm 0.04$	$0.36 \pm 0.05$	0.6	0.02
$\langle f_{\text{H}_2} \rangle$	$0.12 \pm 0.07$	$0.24 \pm 0.09$	0.6	0.02

ies with high SFR, SFE, and  $L_{\text{IR}}$  present high  $L'(^{12}\text{CO})/L'(^{13}\text{CO})$  line luminosity ratios most probably due to younger starburst activity. These higher ratios found here are in good agreement with scenarios in which galaxies with higher fractions of dense molecular gas (see Tables 7 and 10) show higher  $L_{\text{IR}}$  and higher SFE (Solomon, Downes & Radford 1992; Solomon & Vanden Bout 2005), probably induced by the triggering of a recent starburst episode after the infall of unprocessed gas to the central galaxy regions (Casoli, Dupraz & Combes 1992a; Henkel & Mauersberger 1993; König et al. 2016).

Similarly, the  $I(^{13}\text{CO})/I(\text{C}^{18}\text{O})$  line intensity ratios are explained in terms of either a  $^{13}\text{CO}$  deficit or an overabundance of  $\text{C}^{18}\text{O}$ . Recently, low  $I(^{13}\text{CO})/I(\text{C}^{18}\text{O})$  line intensity ratios have been reported for different types of galaxies (Danielson et al. 2013; Jiménez-Donaire et al. 2017; Sliwa et al. 2017; Brown & Wilson 2019). In all these cases, the low ratios have been attributed to the presence of massive stars in a recent starburst. Our trends found for  $L'(^{13}\text{CO})/L'(\text{C}^{18}\text{O})$  (Fig. 10) are in good agreement to previous ratios reported for starburst galaxies (Jiménez-Donaire et al. 2017; Zhang et al. 2018). Considering the 24 VALES galaxies with  $\text{C}^{18}\text{O}$  spectral coverage, we show moderate trends of  $L'(^{13}\text{CO})/L'(\text{C}^{18}\text{O})$  with  $L_{\text{IR}}$ , SFR, and SFE. Galaxies with higher  $L_{\text{IR}}$ , SFR, and SFE are found to show high  $L'(^{12}\text{CO})/L'(^{13}\text{CO})$  (Fig. 9), low  $L'(^{13}\text{CO})/L'(\text{C}^{18}\text{O})$  (Fig. 10) luminosity ratios, and relatively high reservoirs of molecular gas (see Table 10). Similar results have been associated with a top-heavy IMF (Danielson et al. 2013; Sliwa et al. 2017; Zhang et al. 2018; Brown & Wilson 2019); however, in order to break

the degeneracy between young starburst and top-heavy IMF, an independent determination of the age of the starburst is needed.

### 5.1 Optical depth, selective photodissociation, and chemical fractionation effects

Aalto et al. (1995) pointed out the difficulties from interpreting the  $^{12}\text{CO}$  and  $^{13}\text{CO}$  abundances from  $I(^{12}\text{CO})/I(^{13}\text{CO})$  line intensity ratios as these might be affected by surface density, optical depth, and gas temperature. They suggested that the high  $I(^{12}\text{CO})/I(^{13}\text{CO})$  line intensity ratios observed in mergers and interacting galaxies (Casoli et al. 1992b; Henkel & Mauersberger 1993) are produced by the infalling of unprocessed gas that could affect the gas elemental abundances, only if the ISM has moderate optical depths ( $\tau \approx 1$ ). More recently, Zhang et al. (2018) presented how  $^{13}\text{CO}$  and  $\text{C}^{18}\text{O}$  opacity affects  $I(^{12}\text{CO})/I(^{13}\text{CO})$  and  $I(^{13}\text{CO})/I(\text{C}^{18}\text{O})$  line intensity ratios in local thermodynamic equilibrium (LTE) and non-LTE conditions assuming: representative Galactic abundance ratios ( $^{13}\text{CO}/\text{C}^{18}\text{O} = 7\text{--}10$ ,  $^{12}\text{CO}/^{13}\text{CO} = 70$ ), and typical ULIRG and SMG conditions (e.g.  $\tau_{^{12}\text{CO}} \approx 2$ ,  $T_{\text{kin}} = 30$  K). They found that the high  $I(^{12}\text{CO})/I(^{13}\text{CO})$  ratios  $\geq 30$  observed in high-redshift galaxies would need extremely low optical depths for  $^{13}\text{CO}$  ( $\tau < 0.03$ ), meaning that  $I(^{12}\text{CO})/I(^{13}\text{CO})$  line intensity ratios are affected by optical depth effects. In order to properly account the optical depths in  $I(^{12}\text{CO})/I(^{13}\text{CO})$  intensity ratios, multiple line transitions observations are needed to measure excitation conditions and derive the optical depths of the ISM in these galaxies, which is beyond the scope this work and hence, the  $L'(^{12}\text{CO})/L'(^{13}\text{CO})$  luminosity ratios reported here should be taken as a lower limit of the  $^{12}\text{CO}/^{13}\text{CO}$  abundance ratio (Henkel et al. 2010; Martín et al. 2019). On the other hand, Zhang et al. (2018) found that even moderate  $^{13}\text{CO}$  optical depths ( $\tau_{^{13}\text{CO}} \sim 0.2\text{--}0.5$ ) do not cause the  $I(^{13}\text{CO})/I(\text{C}^{18}\text{O})$  line intensity ratio to deviate significantly from more typical values ( $^{13}\text{CO}/\text{C}^{18}\text{O} \sim 7$ ), meaning that the low  $I(^{13}\text{CO})/I(\text{C}^{18}\text{O})$  found in high-redshift starbursts and local ULIRGs reflect the intrinsic isotopologue abundance ratios [i.e.  $I(^{13}\text{CO})/I(\text{C}^{18}\text{O}) \approx ^{13}\text{CO}/\text{C}^{18}\text{O} \approx ^{13}\text{C}/^{18}\text{O}$ ].

If chemical fractionation is the main physical mechanism controlling the observed line ratios, the  $^{13}\text{CO}$  abundance would be boosted with respect to  $^{12}\text{CO}$  (and  $\text{C}^{18}\text{O}$ ) at low temperatures ( $T \approx 10$  K; Watson, Anicich & Huntress 1976). Nevertheless, considering a mean temperature  $T > 20$  K (Ibar et al. 2015; Hughes et al. 2017) for our VALES sample, we can reject chemical fractionation as the main mechanism controlling the  $L'(^{12}\text{CO})/L'(^{13}\text{CO})$  ratios. On the other

hand, selective photodissociation can affect the less abundant  $^{13}\text{CO}$  and  $\text{C}^{18}\text{O}$  molecules compared to  $^{12}\text{CO}$ ; however, extreme conditions with high gas densities ( $>10^{26}\text{ cm}^{-3}$ ) are required (Romano et al. 2017; Zhang et al. 2018). However, with an average gas density of  $10^4\text{ cm}^{-3}$  (Hughes et al. 2017), our sample of galaxies does not fulfil such conditions. Moreover, knowing that  $\text{C}^{18}\text{O}$  is even more sensitive to selective dissociation than  $^{13}\text{CO}$ ,  $\text{C}^{18}\text{O}$  molecules would be more dissociated than  $^{13}\text{CO}$  molecules, resulting in high  $L'(^{13}\text{CO})/L'(\text{C}^{18}\text{O})$  ratios, which is inconsistent with results shown in Fig. 10 where galaxies with more intense UV radiation fields associated with high  $L_{\text{IR}}$  and SFR show low  $L'(^{13}\text{CO})/L'(\text{C}^{18}\text{O})$  ratios. Thus, the  $(L'^{12}\text{CO})/(L'^{13}\text{CO})$  and  $(L'^{13}\text{CO})/L'(\text{C}^{18}\text{O})$  variations found here are not compatible with a scenario in which selective photodissociation or chemical fractionation plays a dominant role.

## 5.2 Insights from Galactic chemical evolution

Recently, Romano et al. (2017) used Galactic Chemical Evolution models to compute the abundances of numerous elements including  $^{12}\text{C}$ ,  $^{16}\text{O}$ ,  $^{13}\text{C}$ , and  $^{18}\text{O}$  in the ISM of galaxies, assuming that (i) stars form from raw material with primordial chemical composition, (ii) outflows remove stellar ejecta and a fraction of the surrounding ISM, (iii) star formation follows a canonical Kennicutt–Schmidt law (Schmidt 1959; Kennicutt 1998), (iv) stars release the synthesized elements during their lifetime, and (v) stellar ejecta are homogeneously mixed in the ISM, allowing us to follow multiple isotopic ratios and trace their abundance ratios on different isotopes and different elements. They have shown that neither selective photodissociation nor chemical isotope-dependent fractionation can significantly perturb globally averaged isotopologue abundance ratios, since these processes will typically affect only small mass fractions of individual molecular clouds in galaxies. Using these models, Zhang et al. (2018) were able to compare the effects of assuming different IMFs of young starbursts by incorporating the appropriate time-scales at which different stellar populations enrich the ISM, and conclude that a canonical IMF cannot reproduce the observed low  $I(^{13}\text{CO})/I(\text{C}^{18}\text{O})$  ratios in ULIRGs and SMGs. Thus, assuming that the velocity-integrated line flux densities coming from average stacks are not affected by these two other effects, we propose that these emission line ratios could be induced by selective nucleosynthesis.

## 6 CONCLUSIONS

In this paper, we present a stacking analysis of  $^{12}\text{CO}(1-0)$ ,  $^{13}\text{CO}(1-0)$  emission lines of 27 galaxies, and  $\text{C}^{18}\text{O}(1-0)$  in 24 galaxies, belonging to the VALES survey. We have detected six individual  $^{13}\text{CO}(1-0)$  line signals from six galaxies in moment-0 maps, with  $\text{SNR} > 5$ . We have successfully demonstrated that it is possible to detect the signal coming from faint emission lines ( $^{13}\text{CO}$  and  $\text{C}^{18}\text{O}$ ) in low-redshift galaxies through stacking analysis, pushing the current ALMA detectability limits. Therefore, the analysis presented here can be applied to detect faint signals from different molecules coming from low-, intermediate-, and high-redshift galaxies, exploiting radio interferometric data sets from ALMA.

We have explored three different independent stacking analyses, two of them in the ‘image plane’ (i) 2D-moment-0 stacking and (ii) 3D-image stacking, while a third one in visibility’s space (iii)  $uv$ -plane stacking. We found that for bright emission line (as the case for  $^{12}\text{CO}$ )  $uv$ -plane stacks produce the highest signal-to-noise compared to 2D-moment-0 and 3D-image stacks. Moment-zero stacked maps

for faint lines, like  $^{13}\text{CO}$ , show the highest signal to noise compared with 3D-image and  $uv$ -plane stackings.

We found an overall  $L'(^{12}\text{CO})/L'(^{13}\text{CO})$  line luminosity ratio of  $16.1 \pm 2.5$ . We also found a dependence of  $L'(^{12}\text{CO})/L'(^{13}\text{CO})$  line luminosity ratio on optical morphology/environment where galaxies showing a close projected companion and mergers show boosted  $L'(^{12}\text{CO})/L'(^{13}\text{CO})$  line luminosity ratios. Mergers show at low significance an  $L'(^{12}\text{CO})/L'(^{13}\text{CO})$  line luminosity ratio that is 2 times higher than that found in galaxies without a projected companion. We also found positive trends between  $L'(^{12}\text{CO})/L'(^{13}\text{CO})$  line luminosity ratio and SFR, SFE,  $L_{\text{IR}}$ ,  $\Sigma_{\text{H}_2}$ , and  $\Sigma_{\text{SFR}}$ .

We also provide  $\text{C}^{18}\text{O}$  stacking analysis for 24 VALES galaxies. We detect signal coming from the 2D moment-0 stacked images at a significance of  $\sim 5\sigma$  with an average  $L'(^{13}\text{CO})/L'(\text{C}^{18}\text{O})$  line luminosity ratio of  $2.5 \pm 0.6$ . This average value is in good agreement to the  $I(^{13}\text{CO})/I(\text{C}^{18}\text{O}) = 3.4 \pm 0.9$  line ratio for starburst galaxies found by Jiménez-Donaire et al. (2017). We find negative trends of  $L'(^{13}\text{CO})/L'(\text{C}^{18}\text{O})$  as a function of  $L_{\text{IR}}$ , SFR, and SFE.

We recall that our  $L'(^{12}\text{CO})/L'(^{13}\text{CO})$  ratios can be affected by optical depth effects, and hence the  $L'(^{12}\text{CO})/L'(^{13}\text{CO})$  luminosity ratios reported here should be taken as a lower limit for the  $^{12}\text{CO}/^{13}\text{CO}$  abundance ratio. To assess the optical depth effects on  $I(^{12}\text{CO})/I(^{13}\text{CO})$  intensity ratios, multiple line transitions observations are needed to measure excitation conditions and derive the optical depths of the ISM.

Neither chemical fractionation nor selective photodissociation is expected to be responsible for the trends found in this work as the required low temperatures ( $\leq 10\text{ K}$ ) and high densities ( $>10^{26}\text{ cm}^{-3}$ ) are not fulfilled by our sample of galaxies. The combined  $L'(^{12}\text{CO})/L'(^{13}\text{CO})$  and  $L'(^{13}\text{CO})/L'(\text{C}^{18}\text{O})$  variations provide additional evidence inconsistent with selective photodissociation as the responsible agents behind the results shown here. This leaves selective nucleosynthesis to be the most probable mechanism for the high  $L'(^{12}\text{CO})/L'(^{13}\text{CO})$  and low  $L'(^{13}\text{CO})/L'(\text{C}^{18}\text{O})$  ratios found in bright far-IR luminosity galaxies. The scenario might be that higher molecular gas reservoirs can trigger new starburst events where high-mass stars enrich their ISM.

Future analyses using ALMA observations of these and other CNO isotopologue molecules ( $\text{C}^{17}\text{O}$ ,  $^{12}\text{CN}$ , and  $^{13}\text{CN}$ ) on larger samples, sampling different galaxy populations covering wider ranges in SFR, SFE, and molecular gas contents at different epochs, could fill in the gap of these molecular line observations between nearby galaxies and lensed galaxies at high redshifts, shedding light on the physical processes behind their star formation activity.

## ACKNOWLEDGEMENTS

We thank an anonymous referee for constructive comments and suggestions, which helped to improve the manuscript. HMH and EI acknowledge partial support from National Fund for Scientific and Technological Research of Chile (FONDECYT) through grant no. 1171710. MJM acknowledges the support of the National Science Centre, Poland through the SONATA BIS grant 2018/30/E/ST9/00208. KKK acknowledges support from the Swedish Research Council (2015-05580). This work also benefited from the International Space Science Institute (ISSI/ISSI-BJ) in Bern and Beijing, thanks to the funding of the team ‘Chemical abundances in the ISM: the litmus test of stellar IMF variations in galaxies across cosmic time’ (principal investigator D.R. and Z.-Y.Z.). TMH acknowledges the support from the Chinese Academy of Sciences (CAS) and the National Commission for Scientific and Technological



Research of Chile (CONICYT) through a CAS-CONICYT Joint Postdoctoral Fellowship administered by the CAS South America Center for Astronomy (CASSACA) in Santiago, Chile. This paper makes use of the following ALMA data: ADS/JAO.ALMA 2013.1.00530.S. ALMA is a partnership of ESO (representing its member states), NSF (USA), and NINS (Japan), together with NRC (Canada), NSC and ASIAA (Taiwan), and KASI (Republic of Korea), in cooperation with the Republic of Chile. The Joint ALMA Observatory is operated by ESO, AUI/NRAO, and NAOJ. GAMA is a joint European–Australasian project based around a spectroscopic campaign using the Anglo-Australian Telescope. The GAMA input catalogue is based on data taken from the SDSS and the UKIRT Infrared Deep Sky Survey. Complementary imaging of the GAMA regions is being obtained by a number of independent survey programmes including GALEX MIS, VST KiDS, VISTA VIKING, WISE, Herschel-ATLAS, GMRT, and ASKAP providing UV-to-radio coverage. GAMA is funded by the STFC (UK), the AAO (Australia), the AAO, and the participating institutions. The GAMA website is <http://www.gama-survey.org/>. This research made use of ASTROPY,<sup>3</sup> a community-developed core PYTHON package for Astronomy (Astropy Collaboration 2013, 2018).

## DATA AVAILABILITY

The data underlying this article are available in the ALMA Science Archive at <https://almascience.nrao.edu/asax/>, and can be accessed with the Project ID: 2013.1.00530.S.

## REFERENCES

- Aalto S., Black J. H., Johansson L. E. B., Booth R. S., 1991, *A&A*, 249, 323  
Aalto S., Booth R. S., Black J. H., Johansson L. E. B., 1995, *A&A*, 300, 369  
Adelman-McCarthy J. K. et al., 2008, *ApJS*, 175, 297  
Alatalo K. et al., 2015, *MNRAS*, 450, 3874  
Astropy Collaboration, 2013, *A&A*, 558, A33  
Astropy Collaboration, 2018, *AJ*, 156, 123  
Bartelmann M., White S. D. M., 2003, *A&A*, 407, 845  
Bera A., Kanekar N., Weiner B. J., Sethi S., Dwarakanath K. S., 2018, *ApJ*, 865, 39  
Bergin E. A., Tafalla M., 2007, *ARA&A*, 45, 339  
Berry M. et al., 2012, *ApJ*, 749, 4  
Bolatto A. D., Wolfire M., Leroy A. K., 2013, *ARA&A*, 51, 207  
Brown T., Wilson C. D., 2019, *ApJ*, 879, 17  
Carvajal R. et al., 2020, *A&A*, 633, A160  
Casoli F., Dupraz C., Combes F., 1992a, *A&A*, 264, 49  
Casoli F., Dupraz C., Combes F., 1992b, *A&A*, 264, 55  
Chabrier G., 2003, *ApJ*, 586, L133  
Cheng C. et al., 2018, *MNRAS*, 475, 248  
Condon J. J., Ransom S. M., 2016, *Essential Radio Astronomy*, Princeton University Press, Princeton, NJ  
Cormier D. et al., 2018, *MNRAS*, 475, 3909  
Danielson A. L. R. et al., 2013, *MNRAS*, 436, 2793  
Davis T. A., 2014, *MNRAS*, 445, 2378  
Dole H. et al., 2006, *A&A*, 451, 417  
Driver S. P. et al., 2016, *MNRAS*, 455, 3911  
Duivenvoorden S. et al., 2020, *MNRAS*, 491, 1355  
Eales S. et al., 2010, *PASP*, 122, 499  
Encarnaz P. J., Stark A. A., Combes F., Wilson R. W., 1979, *A&A*, 78, L1  
Evans N. J., 1999, *ARA&A*, 37, 311  
Fudamoto Y. et al., 2020, *MNRAS*, 491, 4724  
Fujimoto S. et al., 2018, *ApJ*, 861, 7

- Fujimoto S. et al., 2019, *ApJ*, 887, 107  
Gao Y., Solomon P. M., 2004, *ApJ*, 606, 271  
Henkel C., Mauersberger R., 1993, *A&A*, 274, 730  
Henkel C., Downes D., Weiß A., Riechers D., Walter F., 2010, *A&A*, 516, A111  
Herrera-Camus R. et al., 2015, *ApJ*, 800, 1  
Hughes T. M. et al., 2017, *A&A*, 602, A49  
Ibar E. et al., 2013, *MNRAS*, 434, 3218  
Ibar E. et al., 2015, *MNRAS*, 449, 2498  
Jiménez-Donaire M. J. et al., 2017, *ApJ*, 836, L29  
Kennicutt R. C., 1998, *ApJ*, 498, 541  
Knudsen K. K. et al., 2005, *ApJ*, 632, L9  
König S., Aalto S., Müller S., Gallagher J. S., Beswick R. J., Xu C. K., Evans A., 2016, *A&A*, 594, A70  
Langer W. D., Penzias A. A., 1990, *ApJ*, 357, 477  
Lehmer B. D. et al., 2007, *ApJ*, 657, 681  
Lindroos L., Knudsen K. K., Vlemmings W., Conway J., Martí-Vidal I., 2015, *MNRAS*, 446, 3502  
Liske J. et al., 2015, *MNRAS*, 452, 2087  
Loomis R. A., Öberg K. I., Andrews S. M., Walsh C., Czekala I., Huang J., Rosenfeld K. A., 2018, *AJ*, 155, 182  
Martín S., Müller S., Henkel C., Meier D. S., Aladro R., Sakamoto K., van der Werf P. P., 2019, *A&A*, 624, A125  
Milam S. N., Savage C., Brewster M. A., Ziurys L. M., Wyckoff S., 2005, *ApJ*, 634, 1126  
Millard J. S. et al., 2020, *MNRAS*, 494, 293  
Miller N. A. et al., 2008, *ApJS*, 179, 114  
Miller N. A. et al., 2013, *ApJS*, 205, 13  
Mirabel I. F., Sanders D. B., 1989, *ApJ*, 340, L53  
Narayanan D., Krumholz M. R., 2014, *MNRAS*, 442, 1411  
Penzias A. A., Jefferts K. B., Wilson R. W., 1971, *ApJ*, 165, 229  
Perger K., Frey S., Gabányi K. É., Tóth L. V., 2019, *MNRAS*, 490, 2542  
Rickard L. J., Blitz L., 1985, *ApJ*, 292, L57  
Rickard L. J., Palmer P., Morris M., Zuckerman B., Turner B. E., 1975, *ApJ*, 199, L75  
Rigby J. R. et al., 2018, *ApJ*, 853, 87  
Rodighiero G. et al., 2015, *ApJ*, 800, L10  
Romano D., Matteucci F., Zhang Z.-Y., Papadopoulos P. P., Ivison R. J., 2017, *MNRAS*, 470, 401  
Schinnerer E. et al., 2007, *ApJS*, 172, 46  
Schmidt M., 1959, *ApJ*, 129, 243  
Scoville N. et al., 2007, *ApJS*, 172, 1  
Sliwa K., Wilson C. D., Matsushita S., Peck A. B., Petitpas G. R., Saito T., Yu M., 2017, *ApJ*, 840, 8  
Solomon P. M., Vanden Bout P. A., 2005, *ARA&A*, 43, 677  
Solomon P. M., Downes D., Radford S. J. E., 1992, *ApJ*, 387, L55  
Spilker J. S. et al., 2014, *ApJ*, 785, 149  
Taniguchi Y., Ohya Y., 1998, *ApJ*, 507, L121  
Taniguchi Y., Ohya Y., Sanders D. B., 1999, *ApJ*, 522, 214  
Villanueva V. et al., 2017, *MNRAS*, 470, 3775  
Watson W. D., 1977, *CNO Isotopes in Astrophysics*, Vol. 105. Springer, Dordrecht  
Watson W. D., Anicich V. G., Huntress W. T., 1976, *ApJ*, 205, L165  
Webb T. M. et al., 2003, *ApJ*, 582, 6  
Wilson T. L., Rood R., 1994, *ARA&A*, 32, 191  
Wilson R. W., Jefferts K. B., Penzias A. A., 1970, *ApJ*, 161, L43  
Yang G. et al., 2018, *MNRAS*, 475, 1887  
Yen H.-W., Koch P. M., Liu H. B., Puspitaningrum E., Hirano N., Lee C.-F., Takakuwa S., 2016, *ApJ*, 832, 204  
Young J. S., Sanders D. B., 1986, *ApJ*, 302, 680  
Zhang Z.-Y., Romano D., Ivison R. J., Papadopoulos P. P., Matteucci F., 2018, *Nature*, 558, 260

<sup>3</sup><http://www.astropy.org>

This paper has been typeset from a  $\text{\LaTeX}$  file prepared by the author.